Hadronenproduktion in Proton-Proton Kollisionen

MASTER THESIS

Markus Fasel

Betreuer: Prof. Dr. Peter Braun-Munzinger

Institut für Kernphysik

TU Darmstadt

Gesellschaft für Schwerionenforschung

31. Juli 2008

Contents

Abstract

The ALICE Transition Radiation Detector has Particle Identification and Tracking capabilities. In this Master Thesis the quality of the TRD tracking algorithm is discussed. The tracking efficiency in the momentum region between 0.6 GeV/c and 10 GeV/c has been determined to be at a level of 0.96 for stand alone tracking and at a level of 0.99 for combined stand alone and barrel tracking. Concernig the cluster residuals with respect to tracklets it will be shown for cosmic data taken with one TRD supermodule that the cluster residual in y-direction take a value of $750\mu m$ at a signal/noise level of 39. Using the ALICE Central Barrel Detectors p_T-specta for proton-proton collisions at a Centre of Mass Energy of 10 TeV generated using PYTHIA are discussed for the species electron, proton, pion, muon, kaon, K_s^0 and Λ. It will be shown that the reconstructed p_T-spectra reproduce the Monte-Carlo spectra up to a transverse momentum of 3 GeV/c for K_s^0, 6 GeV/c for Λ, pions and muons, 8 GeV/c for electrons and for protons. Concernig the p_T-spectrum for all charged particles it can be shown that the reconstructed spectrum reproduces the spectrum created by Monte-Carlo tracks up to a transverse momentum of 14 GeV/c.

1

Introduction

1.1 The Quark-Gluon Plasma

Strongly interacting particles are consisting of quarks and gluons. These particles are called hadrons and are described by Quantumchromodynamics (QCD). According to the number of valence quarks hadrons can be divided into two groups: Mesons are consisting of a quark-antiquark pair, baryons of three quarks respectively three anti-quarks for the antiparticle. Since quarks are known to carry spin-1/2, baryons are fermions and mesons are bosons. The structure of mesons or baryons can be explained by the color charge, a quantum number of the strong interaction which is carried by quarks and gluons. There are three color charges which are called “red”, “blue” and “green”. All strongly interacting particles appearing in nature have to be color singlets. A color singlet state is existing if either a particle consists of a color-anticolor pair or of a group of three particles where each color is represented. The color wavefunction has to be expressed

$$|\Psi\rangle^{colour} = \frac{1}{\sqrt{3}}\left(|r\bar{r}\rangle + |b\bar{b}\rangle + |g\bar{g}\rangle\right)$$

for mesons and

$$|\Psi\rangle^{colour} = \frac{1}{\sqrt{6}}\left(|rgb\rangle + |gbr\rangle + |brg\rangle - |bgr\rangle - |rbg\rangle - |grb\rangle\right)$$

for baryons. One can see that the color wavefunction is antisymmetric for baryons and symmetric for mesons. A further remarkable property of the

QCD is the running coupling constant. The coupling constant of the strong interaction is expressed in the following way:

$$\alpha_S = \frac{4\pi}{\left(11 - \frac{2}{3}N_f\left(q\right)\right)\ln\left(\frac{q}{\Lambda}\right)} \tag{1.1}$$

with the scale parameter $\lambda = 213^{+38}_{-35}$MeV for 3 quark flavours[6]. According to this, for short distances or large momentum transfer, quarks can be considered as "asymptotic free". In this case, QCD can be described by perturbation theory, which is valid for small coupling constants. For large coupling constants, lattice QCD is employed.

Lattice-QCD calculations however predict that above a certain temperature a phase transition takes place from a hadronic state to a state called the Quark-Gluon Plasma. This temperature is dependent on the baryochemical potential μ_B. At a baryochemical potential close to zero, the critical temperature is approximately 170MeV Above the critical temperature confinement is abolished meaning quarks are no longer bound to hadrons. A further property of Quark-Gluon Plasma is that the chiral symmetry is restored. RHIC experiments show [17] that the Quark-Gluon Plasma behaves like a strongly coupled liquid. Concerning the evolution of high energetic heavy ion collision, the system after the collision thermalizes until the Quark-Gluon Plasma is created. The thermalization proceeds quickly. After the creation of the Quark-Gluon Plasma, the system cools down. When the chemical freeze-out is reached, quarks couple to hadrons. Quark-Gluon Plasma is expected to have existed in the early stage of the universe (until $5\mu s$ after the big bang). With the help of high energy heavy ion collisions (like at SPS, RHIC and LHC), Quark-Gluon Plasma can be created.

A simple way to describe the Quark-Gluon Plasma is the usage of the MIT Bag model[10]. This model treats the QCD in a thermodynamical way, applying a boundary condition which expresses confinement. This boundary condition is the bag pressure. In the model, hadrons are described as an ideal Fermi gas of quarks and gluons. The boundary condition is applied by an outer pressure which counters the Fermi pressure and prevents the partons from leaving

the hadron. This leads to a vanishing parton current at the boarder of the hadron $J_\mu|_{r=R} = \langle \bar{q}\gamma_\mu q \rangle$. The energy of the of the N-quarks inside the bag has the following expression:

$$E = \frac{2.04N}{R} + \frac{4\pi}{3} B R^3 \tag{1.2}$$

where the Bag constant B reflects the boundary condition. In the model natural units are taken ($\hbar c = 1$). The Bag constant can be derived from the minimization of the energy of the N-quark system to the following expression:

$$B^{1/4} = \left(\frac{2.04N}{4\pi}\right)^{1/4} \frac{1}{R} \tag{1.3}$$

For a nucleon with a radius of 0.8fm the bag constant can be calculated to $206 MeV/fm^3$. For a hadron in a two-flavour model consisting of up and down quarks and a vanishing gluon mass, the Fermi pressure has the following expression:

$$P = 37 * \frac{\pi^2}{90} T^4 \tag{1.4}$$

In order to calculate the critical temperature, one has to consider that the Bag pressure has to enclose quarks and gluons to hadrons. If the bag pressure cannot compensate the Fermi pressure anymore, than the confinement is broken and the phase transition has taken place. From this the critical temperature is given using the equilibrium of Fermi pressure and Bag pressure:

$$T_C = \left(\frac{90}{\pi^2}\right)^{1/4} B^{1/4} \tag{1.5}$$

Using the value of the Bag constant mentioned above, one gets a critical temperature $T_C = 144$MeV, which is not far away from the critical temperature given above, using lattice calculation.

There are several signatures for the Quark-Gluon Plasma existing, which have already been measured in the experiments at SPS (NA49, NA50 and CERES) and at RHIC (with the experiments STAR, PHENIX, PHOBOS and BRAHMS). One very prominent signature is the strangeness enhancement

with respect to pp-collisions. During the reaction the quark yields reach chemical equilibrium, but due to chiral symmetry restoration the chemical equilibrium for strange and antistrange quarks is at a higher level in a Quark- Gluon Plasma. Experimentally strangeness enhancement can be tested using the ratios between hadron types containing strangeness and hadron types which do not contain strangeness, i.e. K/π-ratios. For the heavy quarks, a signature for the Quark-Gluon Plasma which was observed at SPS and RHIC was the quarkonia suppression. It can be explained qualitatively using the color charge screening formalism of Matsui and Satz[16]. For a $c\bar{c}$-pair created in a Quark- Gluon Plasma, according to the high particle-density the quarks will also observe the color charge of the partons around, so the pair gets broken and the quarks will be separated. During the hadronisation due to the high abundances of quarks with different flavour, the probability for a formation of a J/Ψ is lowered with respect to other hadrons containing charm quarks and the J/Ψ get suppressed. If the temperature increases, also the production yields for $c\bar{c}$-pairs increase, and charm- and anticharm-quarks from different pairs can couple to a J/Ψ during hadronisation if their colour charges are matching. For LHC conditions an enhancement of J/Ψ is predicted [8].
A third signature for the Quark-Gluon Plasma is connected with jets. In case a quark-antiquark pair is produced in hard collisions, the quarks from this pair are loosing energy when passing the hot dense medium. This also lowers the transverse momentum of the quarks. When these particles fragment to jets, the number of partons with a high p_T is lower for jets from a Quark-Gluon plasma with respect to jets from pp-Collisions, since there the partons do not have to pass the dense medium. This phenomenon is called jet-quenching. In order to investigate jet-quenching, one has to trigger on high-energy particles. In practice, the particle with the highest momentum above a certain threshold will give the trigger signal, then particles in a region around the triggering particle have to be found. Then for all the particles the transverse momen-

tum has to determined. Investigations at RHIC have shown the effect of jet quenching.

For the investigation of the early phase of the Quark-Gluon Plasma, direct photons respectively thermal dileptons are very useful since they are able to pass the material unbiased. Direct photons are created by gluon scattering $gq \rightarrow \gamma q$ and quark-antiquark annihilation $q\bar{q} \rightarrow \gamma g$. Dileptons are created by conversion of virtual photons into a lepton pair. In both cases however the background is large. For direct photon the background comes mainly from $\pi\pi$- and $\pi\rho$-reactions, for the direct leptons it results from pion-annihilation and from Drell-Yan processes. Interesting candidates can also be identified by their transverse momentum. For direct photons the interesting region is between 2 and 5 GeV/c[5]. In this region a clear signal from direct photons is expected. Below 2GeV the signal is dominated by photons from the mixed phase. For leptons the region above 1.5GeV and up to 10GeV is of interest [14], since in this the lepton signal from the Quark-Gluon Plasma can be identified and separated from background processes.

To study the properties of the Quark-Gluon Plasma, the elliptic flow is of interest. For the definition of the elliptic flow, a Fourier analysis on the distribution $E\frac{d^3N}{d^3p}$ is done:

$$E\frac{d^3N}{d^3p} = \frac{1}{\pi}\frac{d^2N}{d^2p}\left[1 + 2v_1\cos(\phi) + 2v_2\cos(2\phi)\right] \tag{1.6}$$

where ϕ is the azimuthal angle between the reaction plane, defined by the impact parameter and the beam axis, and transverse momentum. The first harmonic coefficient is called directed flow. It describes the sideward motion of the particles inside the reaction plane[13]. The second coefficient which is called elliptic flow measures the excentricity of the matter distribution during the formation time. The representation of the elliptic flow is the following [9]:

$$v_2 = \left\langle \frac{p_x^2 - p_y^2}{p_t^2} \right\rangle \tag{1.7}$$

Here the x-direction is inside the reaction plane and orthogonal to the beam-direction z, and the y direction is orthogonal to the reaction plane. This

quantity is applicable to study hydrodynamic properties of the Quark-Gluon Plasma. Measurements of the elliptic flow at RHIC have shown that the Quark-Gluon Plasma behaves like a liquid. A further remarkable feature of the elliptic flow is that it carries information about the thermalization process. The investigation of the Quark-Gluon Plasma was started at SPS and RHIC. At LHC, where the centre-of-mass energy and the temperature of the fireball will be considerably higher, the signatures of the Quark-Gluon Plasma will be further investigated. Here ALICE[1] will be the dedicated experiment for the investigation of the Quark-Gluon Plasma. In the next decade a further experiment at FAIR[2] at GSI will join. The experiment is called CBM[3]. Like the experiments at SPS and in contrast to the experiments at RHIC, CBM will be a fixed-target experiment. In comparison to the LHC, the temperature will be lower, the baryochemical potential however will be higher. More information about the Quark-Gluon Plasma and its signatures can be found in [17], [5], [14] and [7].

1.2 Comparison between heavy-ion collisions and proton-proton collisions

An important quantity used to study relativistic heavy ion collisions is the nuclear modification factor R_{AA}. The nuclear modification factor is defined by the ratio[15]:

$$R_{AA} = \frac{\frac{d^2N_{AA}}{dydp_T}}{N_{Coll} * \frac{d^2N_{pp}}{dydp_T}} \tag{1.8}$$

Here particle yield spectra produced in heavy ion collisions are compared to the yields produced in pp-collisions, scaled by the number of binary collisions N_{Coll}. Using the nuclear modification factor it is possible to investigate the behaviour of particles produced in heavy ion collisions: If the nuclear modifi-

[1] A Large Ion Collider Experiment
[2] Facility for Antiproton and Ion Research
[3] Compressed Baryonic Matter

cation factor is smaller than 1, then one says that the species gets suppressed in heavy-ion collisions. For the Quark-Gluon Plasma the nuclear modification factor can be used to study the particle production at the chemical freeze-out. Since the quarks created in the Quark-Gluon Plasma recombine to hadrons at the chemical freeze-out, the nuclear modification factor can also provide information about the earlier stages of the Quark-Gluon Plasma. For the measurement of the nuclear modification factor, besides the centrality and the particle distribution in heavy-ion collisions, also the particle spectra for Proton-Proton collisions have to be well-known.

1.3 The ALICE experiment

The ALICE-Experiment is a dedicated heavy ion experiment at the LHC[4]. The LHC will accelerate protons to an energy of 7 TeV which leads to a Centre of Mass Energy of 14 TeV. In the heavy-ion mode, the LHC will accelerate Lead nuclei to an energy of 5.5 TeV/nucleon. The experiment is designed to study the signature of the quark gluon plasma. Fig. 1.1 shows the experimental setup of the experiment. In order to fulfill the task, the ALICE experiment consist of the following components:

- Tracking detectors:
  - Inner Tracking System (ITS) for tracking and primary vertex finding
  - Time Projection Chamber (TPC) for tracking and particle identification
  - Transition Radiation Detector (TRD) for tracking and electron identification
- For particle identification
  - Time-of-Flight Detector (TOF)
  - High-Momentum-Particle-Identification (HMPID)
- As electromagnetic calorimeters
  - Electromagnetic Calorimeter (EMCAL)

[4] Large Hadron Collider

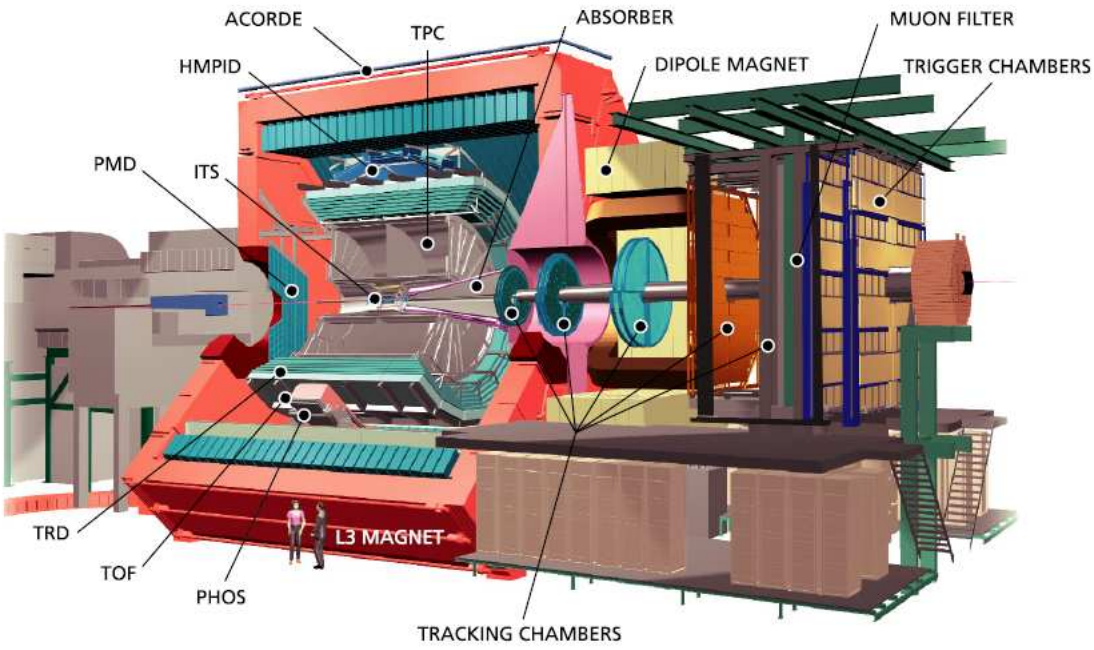

Fig. 1.1: Experimental setup of the ALICE experiment: Schematically shown are the central barrel detectors ITS, TPC, TRD and TOF, the calorimeter PHOS, the Cherenkov counter HMPID, the Forward MUON Spectrometer and the triggering detectors FMD, PMD and ACORDE. Not visible are the electromagnetic calorimeter EMCAL and the triggering detectors V0 and T0. Except for the Foreward MUON Spectrometer, all detectors are placed inside the L3 magnet. Picture taken from [2].

  - Photon Spectrometer (PHOS)
- For muon identification (in forward rapidity region)
  - MUON Spectrometer
- As triggering detectors and for global event characteristics
  - Forward Multiplicity Detector (FMD)
  - Photon Multiplicity Detector (PMD)
  - V0
  - T0
- As cosmic-ray trigger

– ACORDE[5]

The central barrel consists of the detectors ITS, TPC, TRD and TOF. These detectors cover a pseudo rapidity range $|\eta| < 0.9$ with full acceptance in azimuth. The detectors are used for tracking, for primary vertex reconstruction (ITS and TPC) and for particle identification. Other three detectors EMCAL, PHOS and HMPID have to share the acceptance region around the middle plane of the detectors. HMPID is a Ring-Image Cherenkov detector used for the identification of charged particles with a momentum up to 100GeV/c. The purpose of the PHOS detector is to identify γ's and π_0's. EMCAL is a detector created for jet-studies. The Forward MUON Spectrometer will be used for tracking and identification of muons in the forward rapidity region $-4.5 < \eta - 2.5$. The barrel detectors are placed in a homogeneous magnetic field created by the L3 magnet. The strength of the field is $B = 0.5T$
For the first running period starting in august 2008, the status of the main detectors will be the following:

- ITS, TPC, TOF, HMPID and the Forward MUON Detector are completed and ready for data taking.
- TRD will participate with 4 out of 18 supermodules.
- PHOS will participate with 1 out of 5 modules.
- EMCAL will not participate in this run. The detector is planned to be installed in the beginning of the next decade.

The ALICE experiment, its detectors and the measurement tasks are explained in details in [2] and [3].

[5] A Cosmic Ray Detector for ALICE

2

Tracking and Particle Identification with the ALICE Transition Radiation Detector

2.1 Introduction

The ALICE Transition Radiation Detector is placed surrounding the beamline in a distance of 3 meters. It covers a pseudo- rapidity range of $|\eta| < 0.9$ and has an azimuthal acceptance of $360°$. The detector is divided into 18 sectors in rϕ-direction, 5 stacks in z-direction and 6 layers in r direction. Each chamber consists of a radiator, a drift chamber and a padplane for readout. TR-photons are created when charged particles are passing the radiator. The creation of TR-photons is dependent on the Lorentz-factor γ. Photons which are created in the radiator are absorbed in the drift chamber, where they create primary electrons. Also charged particles are creating primary electrons in the drift chamber due to ionization of the gas. Primary electron clusters are moving toward the amplification region, where the signal is read out on the cathode padplane. Fig. 2.1 shows an average pulse height spectra for electrons and for pions at a momentum of 2GeV/c. Besides the main peak corresponding to the amplification region, one can see a second peak for electrons which is due to the absorption of TR-photons.

The main goal of the Transition Radiation Detector is the separation of electrons and pions in a momentum region between 2GeV/c and 10GeV/c with a pion efficiency of less than 1% at 90% electron efficiency. Therefore, the main fields of interest fulfilled with the help of the TRD are single- and di-electron physics, i.e the reconstruction of J/Ψ and Υ in their di-electron decay channel

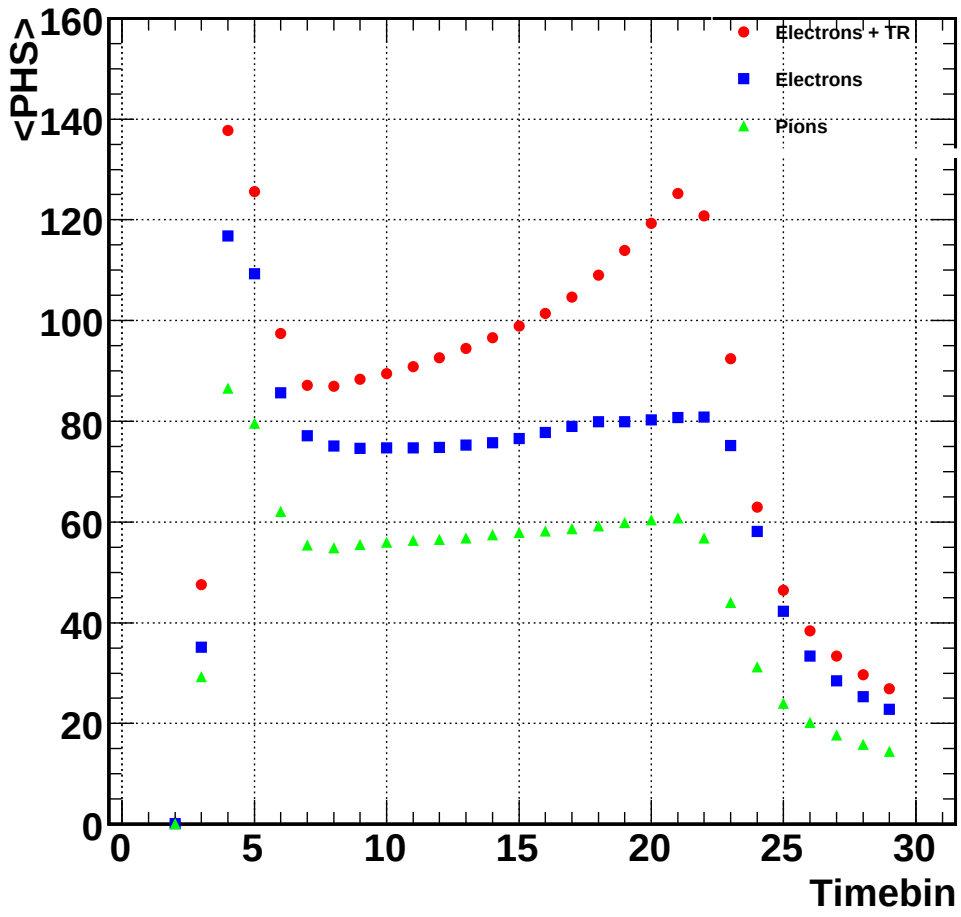

Fig. 2.1: Average pulse height spectrum measured with a prototype of the ALICE Transition Radiation Detector in the testbeam 2004. Shown is the average pulse height over the time bin for electrons and pions using a radiator, and also for electrons where no radiator is used in the setup. The particle momentum was 2GeV/c. Beside the amplification peak, one can identify a second peak for electrons in the setup with radiator. The second peak is produced by TR absorption.

as well as the measurement of the charm and bottom cross sections using single electrons. Also photons can be measured in the TRD via conversions. The TRD can be used as a fast trigger on electrons and jets with a trigger response after $6\mu s$. Further on, the TRD is one of the central barrel tracking detectors.

2.2 Tracking in the ALICE Transition Radiation Detector

The TRD tracking code is discussed in [12]. Tracking in the TRD is performed in two different ways: On the one hand, tracks coming from the TPC are prolonged inside the TRD, and if the tracks are not stopped inside the detector, they are propagated towards TOF. On the other hand, tracking can also be performed inside the TRD by a stand alone tracking algorithm without information coming from other detectors. The two algorithms follow different strategies: barrel tracking is based on Kalman Filter approach[1]: Using the Kalman Filter, a state vector x_k is defined for each point. For the ALICE tracking code, the state vector consists of five parameters: The local y- and z-coordinate, the local sinus of the track momentum, the tangent of the local dip angle and the reciprocal of p_T. Further the covariance matrix C_k according to the state vector is required. The idea behind the Kalman Filter is, once having an estimate of the state vector x_{k-1} and a measurement of the state vector for the next time step y_k, to calculate the estimation of the state vector for the next time step. Doing this, a prediction $\tilde{x}_k^{k-1}$ of the state vector for the next time step has to be calculated according to

$$\tilde{x}_k^{k-1} = f_k(\tilde{x}_{k-1}) \tag{2.1}$$

where f_k describes the evolution of the state vector. Also a prediction for the covariance matrix has to be made:

$$\tilde{C}_k^{k-1} = F_k C_{k-1} F_k^T \tag{2.2}$$

with $F_k = \frac{df_k}{dx_{k-1}}$. The measured state vector is correlated with the real state vector by

$$y_k = H_k x_k + \delta_k \tag{2.3}$$

with the noise δ_k, which has the covariance matrix V_k. It can be shown that the estimation of the state vector x_k can be calculated using the prediction $\tilde{x}_k^{k-1}$ and the measured state vector y_k according to.

$$\tilde{x}_k = \tilde{x}_k^{k-1} * K_k \left(y_k - H_k \tilde{x}_k^{k-1} \right) \tag{2.4}$$

The quantity $K_k = \tilde{C}_k^{k-1} H_k^T \left(V_k + H_k \tilde{C}_k^{k-1} H_k^T \right)^{-1}$ is called Kalman gain. Also the covariance matrix has to be updated using the prediction

$$\tilde{C}_k = \tilde{C}_k^{k-1} - K_k H_k \tilde{C}_k^{k-1} \tag{2.5}$$

The Kalman Filter was implemented in the class AliExternalTrackParams. Here the function PropagateTo creates the prediction for the next step, the function Update calculates the estimate of the new state vector. For the TRD tracking code this means that the measured point for the iteration step has to be created. As measured point the tracklet is used. A tracklet consists of clusters within a chamber which are assumed to be linearly dependent in the $r\phi$-direction with respect to the time. A big advantage of the Kalman Filter based tracking algorithm is that it takes into account energy loss and multiple scattering. A further advantage is that it directly rejects non-matching space-points created by noise.

The core of the stand alone tracking algorithm is a track model which is fitted to the clusters. To get the track model, we start from the equation of a circle in the xy-plane

$$(x - x_0)^2 + (y - y_0)^2 - R^2 = 0 \tag{2.6}$$

where R is the radius of the circle and (x_0, y_0) is the center of the circle, and take into account that the pads are tilted by an angle ϕ_t. The measured y-coordinate is related to the real y-position of the track according to

$$y\prime = y - \tan(\phi_t)(z - z_c) \tag{2.7}$$

where z is the real position of the track and z_c is the z-position of the cluster, which is defined as the center of the pad. For the z-coordinate of the track a linear dependence is assumed:

$$z = d * (x - x_{ref}) + e \tag{2.8}$$

where $d = \frac{dz}{dx}|_{x=x_{ref}}$ and $z = z\left(x_{ref}\right)$ are free parameters of the model. After inserting eq. 2.7 and eq. 2.8 into eq. 2.6, under the assumption that the tilting pad correction can be neglected in quadratic order, we get the equation which serves as the track model:

$$\left(x - x_0\right)^2 + \left(y\prime - y_0\right)^2 - R^2 - 2y_0 \left[\tan\left(\phi\right)\left[d + \left(x - x_{ref}\right) + e\right]\right] = 0 \quad (2.9)$$

In order to fit the equation to the clusters, the equation can be linearized using the following transformation:

$$t = \frac{1}{x^2 + y\prime^2} \quad (2.10)$$

$$u = \frac{2x}{x^2 + y\prime^2} \quad (2.11)$$

$$v = \frac{2\tan\left(\phi_t\right)}{x^2 + y\prime^2} \quad (2.12)$$

$$w = \frac{2\tan\left(\phi_t\right)\left(x - x_{ref}\right)}{x^2 + y\prime^2} \quad (2.13)$$

For the linearized track model we get

$$a + bu + ct + dv + ew - 2\left(y\prime + \tan\left(\phi_t\right) z_c\right) = 0 \quad (2.14)$$

where $a = -\frac{1}{y_0}$, $b = \frac{x_0}{y_0}$ and $c = \frac{x_0^2 + y_0^2 - R^2}{y_0}$. From the parameters, the curvature of the track can be calculated by $\kappa = \frac{a}{\sqrt{1 + b^2 + ca}}$.

Track finding in the stand alone tracking is done in the following way: To start with, a seeding configuration is created out of four seeding clusters. In order to be more robust towards noise, the seeding clusters are the center of gravity of the cluster positions projected to one xy-plane. For the seeding configuration a constraint is made on the angles in y- and z-direction with respect to the x-axis. They have to be less than $45°$. Having the seeding configuration, a circle is fitted to the seeding clusters. Tracklets are created by attaching clusters to the tracklet using the slope coming from the circle fit, and afterwards performing a linear least-square-fit. Having the tracklets, a fit of the track model to the clusters is done in order to reject candidates with a non-sufficient quality. The quality is dependent on the χ^2-value of the fit,

the number of clusters which are attached to the track, and the difference of the slope for all chambers. Tracks which fulfill the quality condition are extrapolated to the chambers which were not taken into account for the seeding so far. The extrapolation is done by creating tracklets using the position and slope calculated from the model fit. Having all the tracklets, the four tracklets with the worst quality are attempted to be improved in an iterative procedure. During each iteration step, each of the four tracklets is rebuild using the position information from the Riemann fit. Afterwards the Riemann fit is done again in order to decide via the χ^2 value of the fit whether an improvement is achieved. If the track quality has improved, then the position information is updated for each tracklet, otherwise the previous tracklet information is taken and the iteration is stopped. In the last step of the generation of the track candidate, the model is fitted again to the final tracklets, and a likelihood value is created. This likelihood value is used in a filter to get the tracks with the best quality. Fig. 2.2 shows an example of the model fitted to clusters both for y- and z-direction. The algorithm is performed iteratively on the set of clusters which are not attached to tracks until in one iteration step no further track is found. Since the track points which are taken to perform the fits are coming from the clusters, and the clusters are "‘aware"’ of calibration and alignment, the tracking algorithm is calibration and alignment aware.

In comparison to the barrel tracking algorithm, the stand alone tracking algorithm has the advantage that it is independent on the TPC. Further on, since the algorithm is based on fitting a circle to track points, the algorithm is fast. By this, the main usage for the stand alone tracking algorithm is the High Level Trigger, where a fast tracking method is necessary to provide a trigger decision. The stand alone tracking algorithm however has the disadvantage that it doesn’t take into account material which the Kalman Filter algorithm does. Effects like multiple scattering inside the material are neglected inside the algorithm. This lead to a degradation of the position and momentum resolution

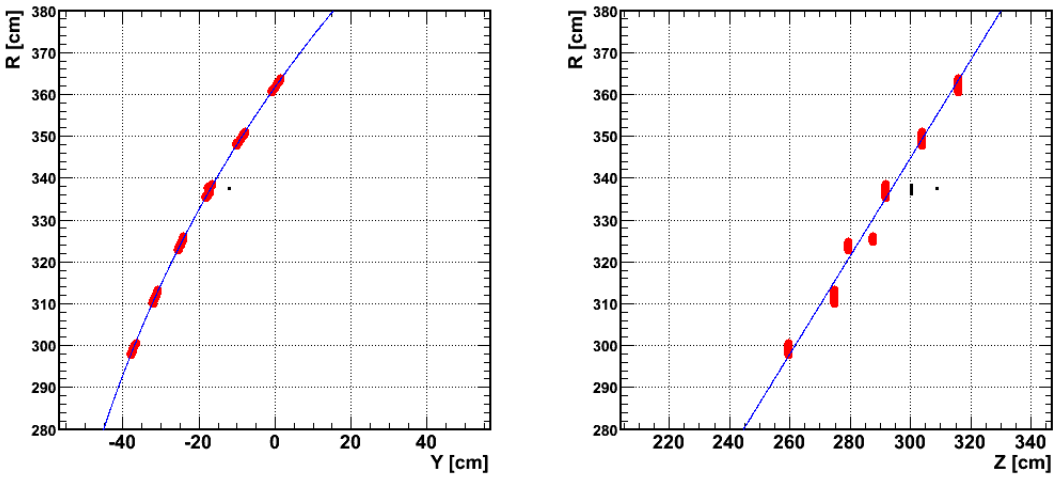

Fig. 2.2: Track found by the stand alone tracker: One can see the track model (blue) fitted to the clusters (red) in one stack. For the y-direction (left) a circle is fitted to the clusters after tilting pad correction. Since the z-direction is connected to the y-direction by the tilting-pad correction, the model for the z-direction is derived by the same fit.

for the stand alone tracking. For the offline analysis, tracks reconstruction by the Kalman Filter are heaving a higher accuracy.

As an option, both trackers can be included in the reconstruction. In a first step, the barrel tracking propagates tracks coming from the TPC. These tracks are marked for the later analysis as tracks form the barrel tracking. One the set of clusters which is not yet attached to any track, stand alone tracking is performed to find also tracks which are not found by the barrel tracking. These tracks are coming from conversions in the material between TPC and the first TRD layer. Approximately 10% of the conversions are happening in this region. Another possibility where tracks are not propagated from the TPC is if the first layer is missing for the reconstruction, i.e. if a half chamber is switched off. Due to the material budget in the TRD the back propagation fails. Due to these cases, it is useful to perform reconstruction with both methods.

2.2.1 Tracking Efficiency

The tracking efficiency, defined as the ratio between the number of reconstructed tracks and the number of findable tracks, was determined with the help of a Monte Carlo sample. The study sample consists of subsamples of particles where all particles were created with the same momentum (0.6 to 10 GeV/c). Each subsample consisted of electrons, pions, kaons, muons and protons.

For the calculation of the tracking efficiency, the Monte-Carlo information has to be compared to the ESD track information. This can be done using the Monte-Carlo label which is assigned to the track. The Monte-Carlo label corresponds to the track number in the Monte-Carlo event. Here only particles which are leaving hits inside the detector are regarded so that the comparison is made with respect to findable tracks. For each Monte-Carlo particle, the corresponding reconstructed track is searched. If it exists, a pair of matching ESD and MC tracks are created. On the other Monte-Carlo tracks, cuts have to be applied to decide whether they are findable or not. Using this information, the ratio of found tracks with respect to findable tracks can be calculated.

The code for calculation of the efficiency is based on the Analysis Framework (see chapter3). For all Monte Carlo particles leaving hits inside the TRD an object which is called AliTRDtrackInfo is created. This objects contains the track references and depending on whether they exist, the TRD track or the external track parameters. A class deriving from AliAnalysisTask is creating the track information objects which are passed to the consumer tasks. These consumer tasks are i.e. calculating the efficiency. The framework is extensible and other tasks like PID efficiency studies or calibration tasks can be added. Fig. 2.3 shows the scheme.

The efficiency was measured in two cases: In the first case the efficiency was measured for tracks found only by the stand alone tracker with respect to all findable tracks for the stand alone tracker. The second tasks compares all the tracks found inside the TRD, either found by the stand-alone tracking or by

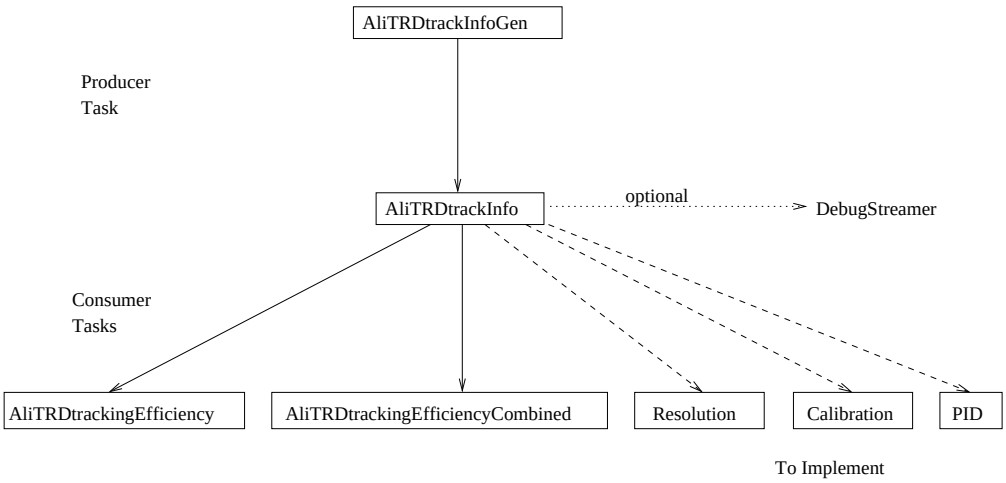

Fig. 2.3: Schematic view of the TRD tracking investigation code. Inside the task AliTRDtrackInfoGen reconstructed tracks and Monte-Carlo tracks are matched using the Monte-Carlo label of each track. The comparison is store in a new object AliTRDtrackInfo. Also for Monte-Carlo tracks where the ESD-track is missing, AliTRDtrackInfo Objects are created if track references inside TRD are found. These objects are stored in a TObjArray and passed to consumer tasks for efficiency calculation.

the barrel tracking, to the number of tracks which are findable for the stand alone tracking. Here also the performance of the barrel tracking is included. In order to get the number of findable tracks, cuts are applied on the momentum, on the number of layers, on the track angles in y- and z- direction and on the sectors. A low-p_T cut at 0.5GeV shall exclude low momenta tracks having a curvature which is too high to be reconstructable. Since the stand alone tracking requires at least four layers to reconstruct a curved track and discards track candidates crossing sectors, the same cuts are chosen for Monte-Carlo tracks. Concerning the track angles Monte Carlo tracks are rejected above an angle of 45° in y- and z-direction, which also matches with the cuts inside the stand alone tracker. A further cut is set on the Monte Carlo tracks to be primary tracks.

Figure 2.4 shows the the measured efficiency for the cases of tracks found by the stand alone tracker only and of tracks found either by stand alone track-

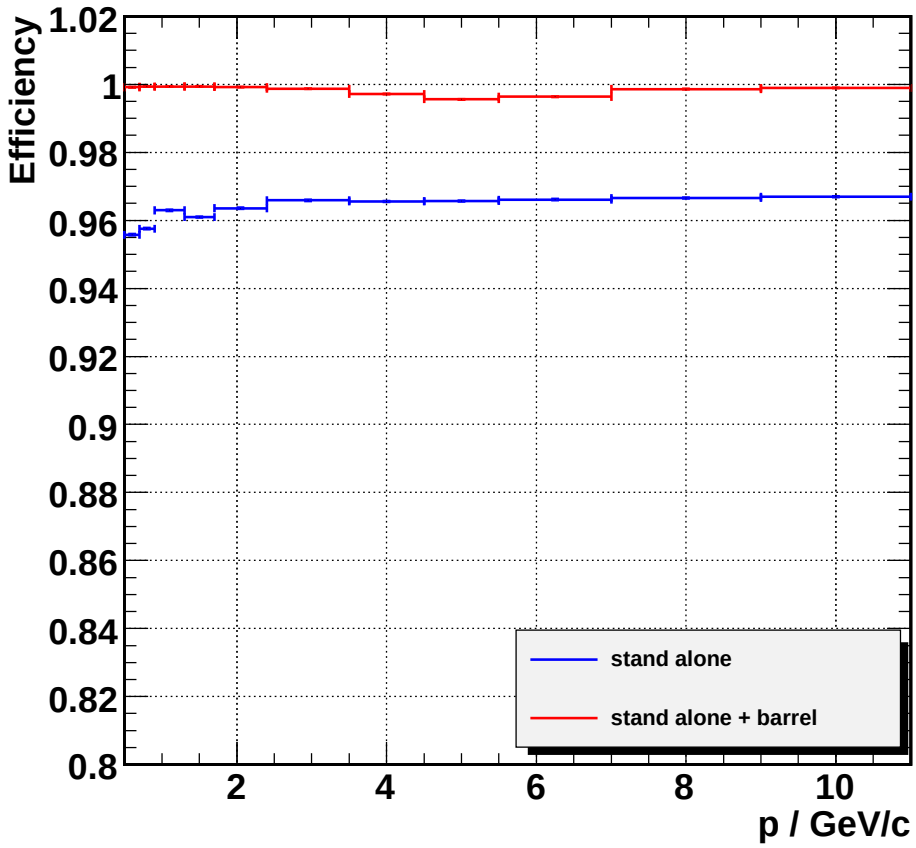

Fig. 2.4: Tracking efficiency calculated as ratio of found tracks with respect to findable tracks: Shown is the efficiency for stand alone tracking and for a combination of stand alone and barrel tracking. One can see a slight increase in the stand alone tracking efficiency. Both stand alone and combined tracking efficiency stay above 90%

ing or barrel tracking with respect to all tracks findable for the stand alone tracker. For both cases the reconstruction was done separately. In order to avoid double counting of tracks, i.e. that a track is found both by the stand alone tracker and the barrel tracking, in the second case also the Monte Carlo label is checked and candidates which are already found are rejected. One can see that for tracks found with the stand alone tracker the efficiency stays at a constant level at 96%. For the combination of stand alone tracking and

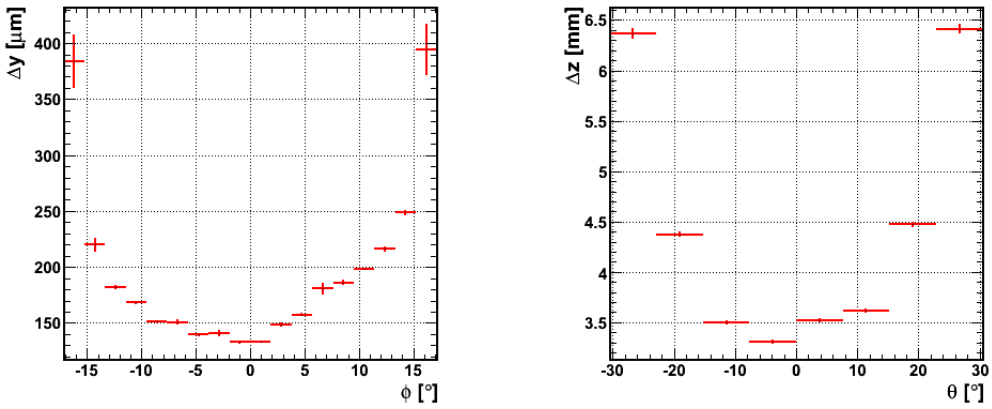

Fig. 2.5: Tracking resolution in y- and -direction as function of the track angles ϕ and θ for particles with a momentum of 3 GeV. One can see a minimum near the angles $\phi = 0°$ respectively $\theta = 0°$. The minimal values are approximately 130 μm in y-direction and 3.3 mm in z-direction

barrel tracking an efficiency of approximately 100% can be reached. As a third case the efficiency can be drawn for all TRD tracks propagated from the TPC which have hits inside the TRD. Here the performance of the back propagation is tested. Here for high momentum tracks an efficiency of 100% can be reached.

2.2.2 Tracking resolution of tracks found by the stand alone tracking

In order to calculate the tracking resolution for stand alone tracking, the measured position of the track is compared with the position derived from the Monte-Carlo information. The Monte-Carlo position information is stored in an object AliTrackReference which is stored when a particle enters and leaves a detector segment (a TRD chamber). In order to access the Monte-Carlo information, the track label of the ESD-track can be used. For the calculation only tracks which are passing all six chambers are taken. The track model is fitted to the tracklets stored in track in order to get the measured position of the track. The distance between measured track position and Monte-Carlo track

Anode Voltage / kV	Number of Events	Number of tracks
1.4	20458	109
1.45	20570	1123
1.5	20425	5368
1.55	20652	10752
1.6	16223	9962

Table 2.1: Run statistics for the runs analysed in order to calculate the cluster residual dependence on the Signal/Noise ratio

position at the beginning and the end of the chamber is defined as tracking resolution.

Fig. 2.5 shows the tracking resolution in y- and z-direction for particles with a momentum of 3 GeV/c. One can see the dependence of the resolution on the track angles ϕ in the xy-plane and θ in the xz-plane. The minimum values which can be found are 130 μm in y-direction and 3.3 mm in z-direction. In comparison to the cluster resolution in z-direction which has a value of 2.3 cm, the improvement of the tracking resolution achieved by the pad tilting is substantial.

2.2.3 Measurement of the Signal/Noise dependence of the cluster residuals using cosmic data

The dependence of the cluster residuals with respect to tracklets defined as the distance between the clusters and the tracklet at the same radial position on the Signal/Noise-value was measured using cosmic ray data taken with supermodule 3 in the cosmic stand in Münster. Supermodule 3 was formerly used for the testbeam measurements. Due to a gas leaks in the chambers, the supermodule had to be disassembled, corrected and reassembled. With the reassembled supermodule cosmic runs with several anode voltages were taken. Anode voltages were chosen between 1.4kV and 1.6kV. The run statistics are shown in Tab.2.1. In previous noise measurements the noise value was determined to 1.5 counts. For the signal the mean value of the average pulse

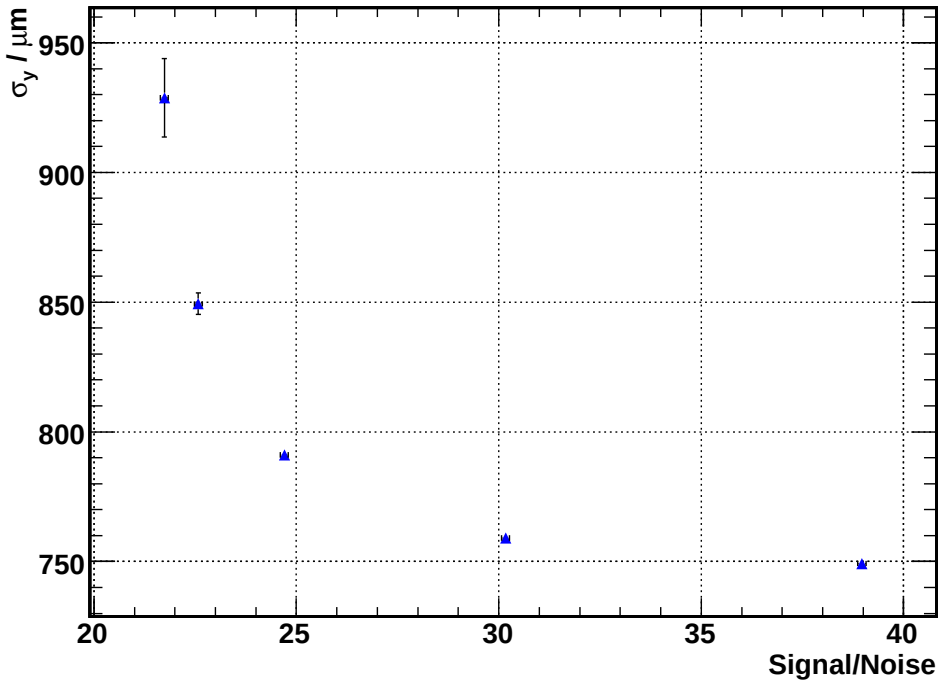

Fig. 2.6: Cluster residuals dependence on the Signal/Noise data: One can see a hyperbolic decline towards higher Signal/Noise ratios. A saturation takes place at the order of 750μm

height spectrum excluding four presamples was taken. The residual value was defined as the σ-value of the distribution of the distances between cluster y-position and tracklet y-position. For this a gaussian fit was applied to the distribution in the Δy-range between -2 and 2mm. Fig.2.6 shows the dependency of the cluster residuals with respect to the Signal/Noise ratio. One can see a hyperbolic decrease with higher Signal/Noise values which saturates at a residual value of 750μm. The relatively high values of the residuals with respect to the previously measured ones[4] are due to several reasons: First the track sample consist of different momenta. Especially low momentum tracks will increase the cluster residuals. Second, the analysis was done on uncalibrated data which also affects the cluster residuals. For this one can expect higher residuals.

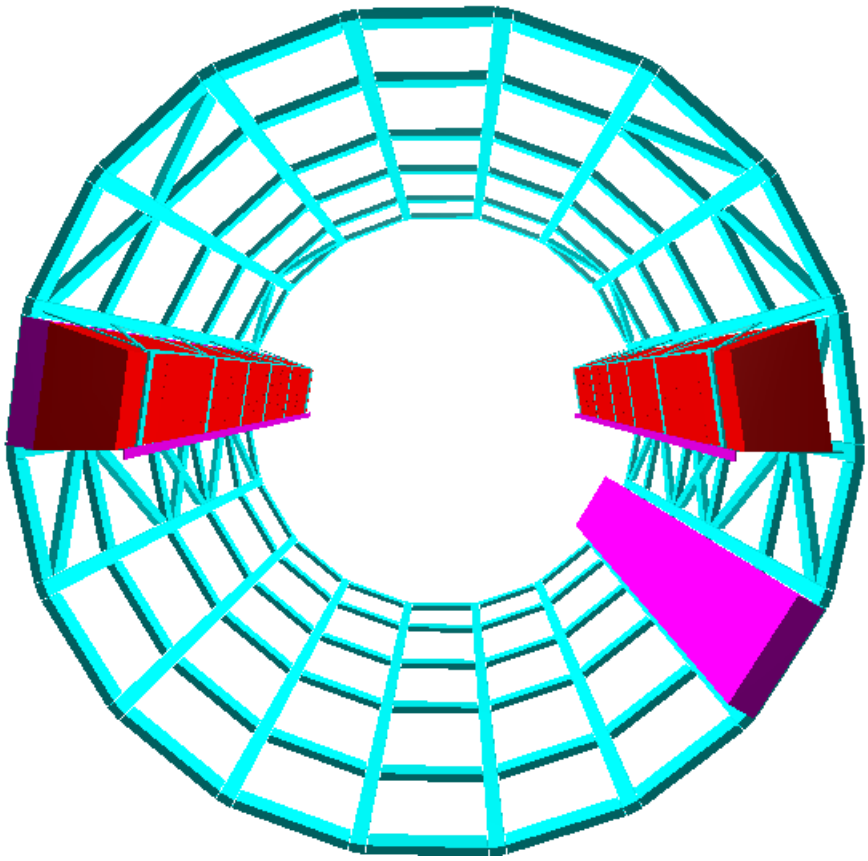

Fig. 2.7: Configuration of TRD and TOF supermodules participating in the cosmic run in February 2008: TRD supermodules(red) are placed in positions 0 and 8, TOF supermodules (violet) in positions 0 and 10. The trigger signal was provided when the two TOF supermodules had a signal in coincidence.

2.2.4 First experimental measurements from the cosmic runs in 2008

In preparation for the running at LHC in 2008, two cosmic runs have been taken place in February and from May on. The main purpose of these cosmic runs is for the detectors to test the subsystems, do calibration tasks and do have alignment runs. TRD also participated in these cosmic runs. During the cosmic run in February 2008, two supermodules (in the sectors 2 and 8) were available, in May two further supermodules were installed in sectors 9 and 17.

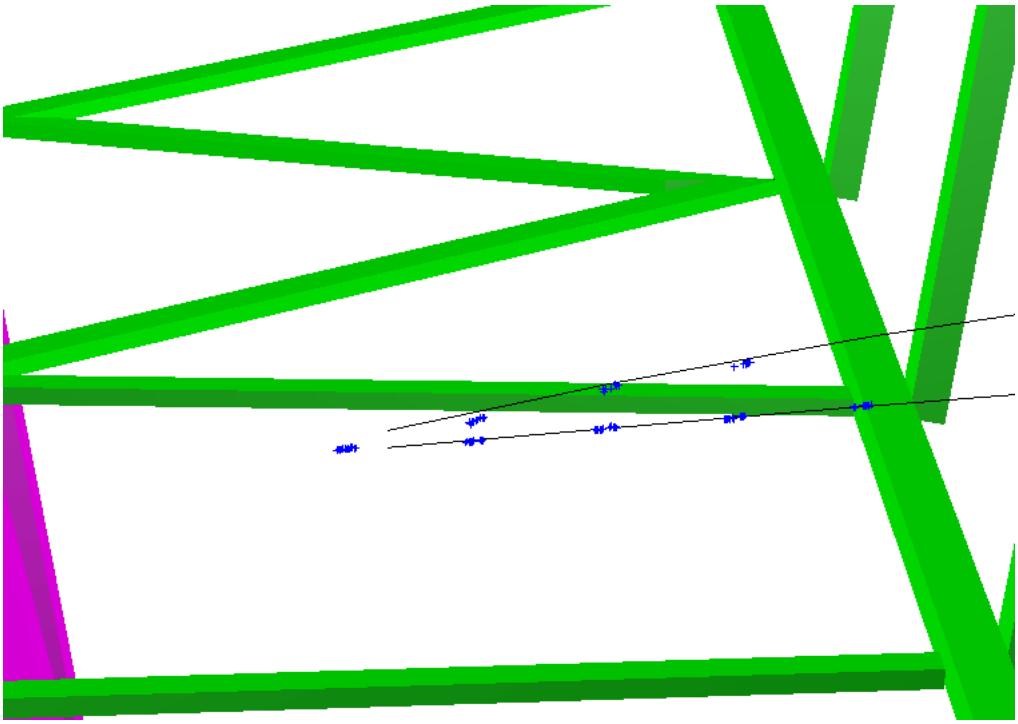

Fig. 2.8: Event taken in the cosmic run in February 2008: One can see 2 tracks in supermodule 0 which are reconstructed by the stand alone tracking. The picture is taken using the ALICE Event Display.

Results form the cosmic run in February 2008

In the February cosmic run, TOF supermodules were serving as cosmic trigger since the probability to find tracks inside the existing TRD supermodules using ACORDE triggered events was very low due to geometrical reasons. The triggering TOF-supermodules were in positions 0 and 10 (Fig.2.7), and trigger signal was provided if the two supermodules had a signal in coincidence. For this setup the trigger efficiency is quite low. Most of the signals provided by the trigger is based on noise or on uncorrelated events. As a drift gas a mixture of Argon and CO_2(82%/18%) was used. All runs taken in the February cosmic run were reconstructed at GSI. All together 156 tracks are found in 24066 events. Fig.2.8 shows an example event with two reconstructed tracks inside the TRD supermodule 0. This shows that the tracker is

Run Number	Number of events	Number of TRD tracks
37051	215464	629
37058	136588	265

Table 2.2: Run statistics of the May cosmic runs: Shown are the run number, the number of events and the number of TRD tracks

working also on experimental data. Due to noise contamination and gas leaks in the two supermodules which leads to an unstable gas situation, these data are of low physical use.

Results from the cosmic run from May 2008

Since both supermodules which are suffering from the gas leak problem are still in the setup, like in the cosmic run in February the gas composition in the TRD chambers in the cosmic run starting in May 2008 is $Ar\ CO_2$. In contrast to xenon, argon is less efficient in TR-absorption. The gas composition will stay for the supermodules installed in the ALICE setup until the these two supermodules are repaired. In May 2008 two further supermodules were installed in sectors 9 and 17, so that in these run TRD participated with four supermodules. The following discussion is based on the runs mentioned in Tab. 2.2. As a trigger either ACORDE or a combination of two TOF-supermodules with one inner supermodule with respect to the LHC ring and one outer supermodule was used. Since for the runs taken so far the pretrigger was not installed for the TRD, the first part of the signal was missing for the tracks. This can be seen from the average pulse height spectrum shown in Fig. 2.9. Here one can see that the first μs of the signal containing the amplification peak is lost due to the late trigger signal. Only a part of the plateau region and the tail is remaining. The second peak one can see at timebin 25 can be explained with noise contamination. The shape of the signal has also consequences on the distribution of the number of clusters attached to tracklets, shown in Fig 2.10. One can see a peak in the number of clusters distribution at around 18 clusters. Since the number of timebins sampled in

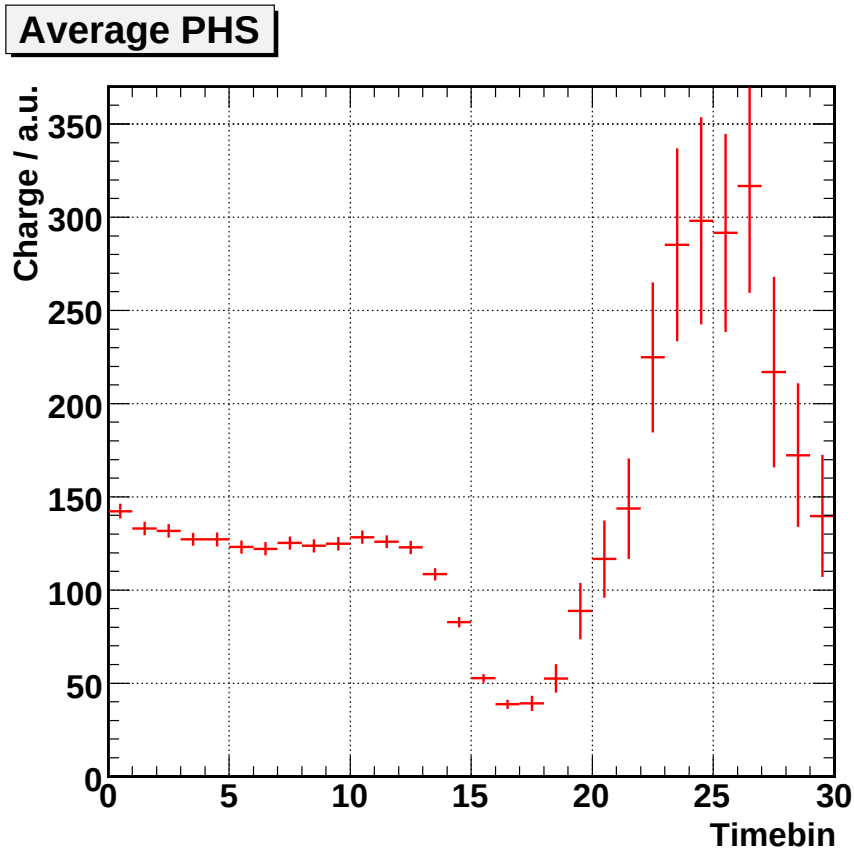

Fig. 2.9: Average Pulse Height Spectrum from cosmic runs 37051 and 37058: One can see that the second part of the average Pulse Height Spectrum is shifted to earlier timebins and that the amplification region is missing. This is due to the fact that the pretrigger was missing for these runs.

this run were 30, the other clusters are missing due to the late trigger signal. Tracks from these events are due to this case usable only for gain calibration and for alignment, but not for resolution studies.

A further quantity describing the quality of the tracks is the number of tracklets per track. Fig. 2.11 left shows the distribution of the number of tracklets found for each track. One can see that most of the tracks have four or five tracklets. The number of tracklets for on track can also be seen from the distribution of the number of clusters (Fig. 2.11 right). One can see peaks at around 60 and 80 clusters per track. Taking into account the distribution of

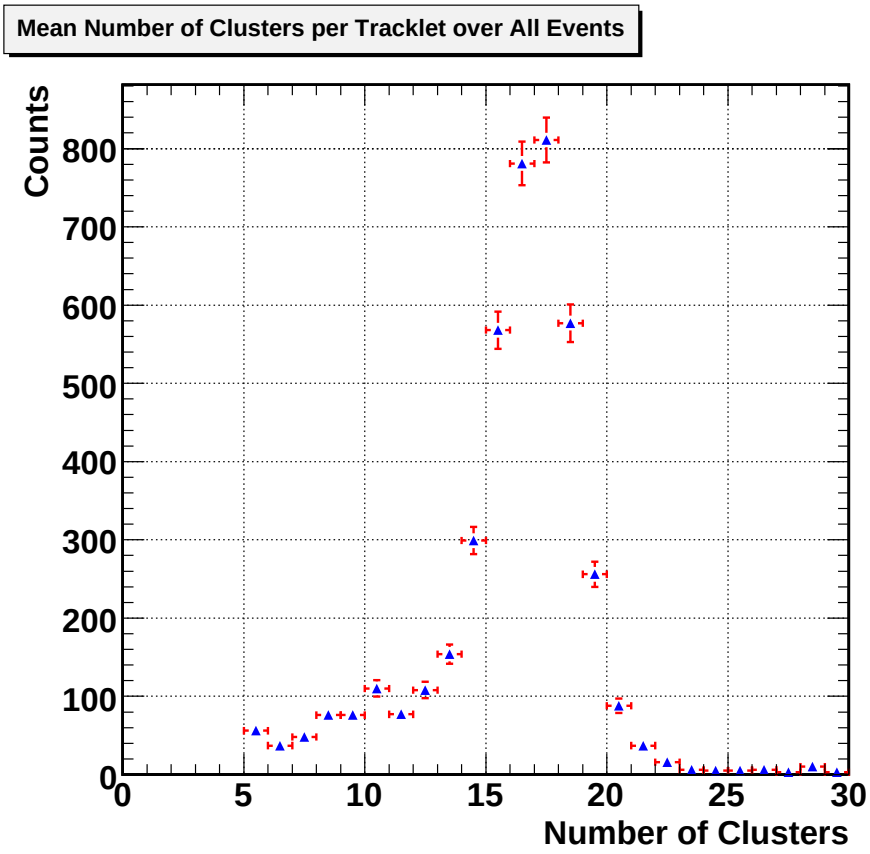

Fig. 2.10: Distribution of the number of clusters in the first may cosmic runs: One can see a sharp peak at around 17 clusters. The lack of the other clusters is due to the missing pretrigger for the TRD

the number of clusters per tracklet shown above, one can identify the peak at 60 clusters per tracklet with tracks having four tracklets and the peak at 80 clusters per track with tracks having five tracklets.

A last quantity to be shown in this context is the χ^2-Distribution of the track normalized to the number of degrees of freedom. The distribution is shown in Fig. 2.12. One can see that most of the entries are below one. The χ^2 value for these tracks is too small. This leads to the conclusion that the errors are overestimated. Concerning this point a better understanding of the data is necessary.

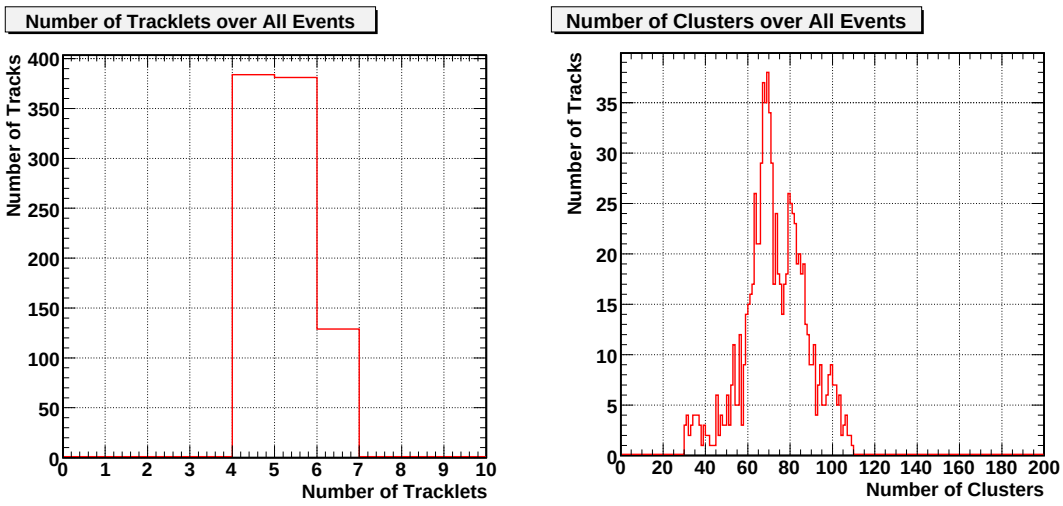

Fig. 2.11: Number of tracklets found for the tracks in the cosmic runs 37051 and 37058: the left picture shows the number of tracklets stored for each track in the ESD file. The right picture show the number of clusters attached to tracks. One can see sharp peaks at 60 and 80 clusters which belong to tracks with 4 and 5 tracklets.

During July the TOF pretrigger will be connected to the TRD trigger system. From the first runs with pretrigger, the measurement of the track quality criterions under real conditions have to be repeated. A more important issue for the time before running is the measurement of the position resolution with respect to the layer and to the track angle on calibrated data using large statistics under operational conditions. This quantity is off high importance for the systematic error.

2.3 Particle Identification with the Transition Radiation Detector

Particle Identification inside the TRD is done based on the charge deposit of a track inside a chamber. The charge deposit is calculated using the charge of the clusters inside the chamber. For each chamber then a PID probability for each of the five species electron, pion, muon, kaon and electron is calculated. The PID for a particle is the product of its PID-probability in all chambers

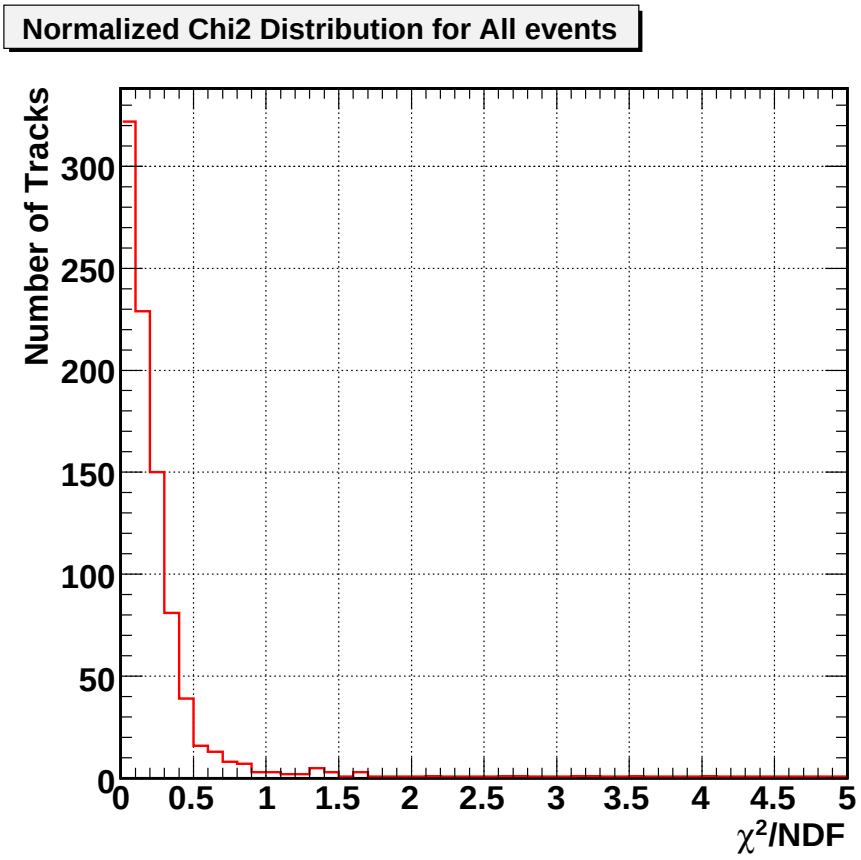

Fig. 2.12: χ^2-Distribution of the cosmic tracks found in the cosmic runs 37051 and 37058: One can see that most of the tracks have a normalized χ^2-value less than 1

normalised by the sum of the PID-probabilities of all particles. In order to get the PID probability for a track in one chamber, the 2-dimensional likelihood method or the neural network method[18] is used. For both methods, the pulse height spectrum has to be divided into several slices: three for the 2-dimensional likelihood method and eight for the neural-network method. In case of the 2-dimensional likelihood method, the classification into three slices reflects amplification region, plateau region and the region of the TR-peak in the average pulse height spectrum.

The calculation of the charge deposit slices as well as the calculation of the PID-probability is performed during tracking. In order to calculate the PID-

probability for each species in one chamber using the two-dimensional likelihood method, a probability value has to be checked inside the two dimensional reference distribution, which exists for discrete momenta and each particle species. To get the PID probability from the reference distribution, the slices two and three have to be combined to one charge deposit value. Together with the charge deposit value of slice one, the probability as function value of both charge deposit values can be derived from the probability distribution.

Due to modifications inside the tracking code which deal with the calculation of the charge deposit value in the chamber, the reference distribution in previous AliRoot versions is not matching with the new tracking code anymore, so it had to be refreshed. In order to create the new reference distribution, a production as described for the efficiency has been done for the reference distributions. This time for each momentum steps 100 runs each containing 100 events were performed. In each event 200 particles were created: for each of the mentioned species and for both particle and antiparticle 20 primaries. All runs were reconstructed with the tracking software where the reference distribution later had to be introduced. The reconstructed tracks were compared with the Monte-Carlo information in order to get the true particle identification. In order to recalculate the charge deposit in each of the three slices, the cluster information stored in the calibration object in the AliESDfriendTrack is used. The calculation of the charge deposit for each slice is done with the same function which is used to calculate the charge deposit during tracking. The values for slice one and the combined value for slices two and three are stored in a 2-dimensional histogram.

Fig. 2.13 shows the 2-dimensional likelihood distributions for electrons and pions. One can see for both distributions a global maximum, which is for electrons at higher charge deposit values in the amplification region as well as in the drift region with respect to the distribution for pions. Also the width of the distribution is larger in both dimensions for electrons with respect to

pions. With the help of the likelihood distributions, electrons and pions can be separated using their charge deposit in the amplification and drift region.

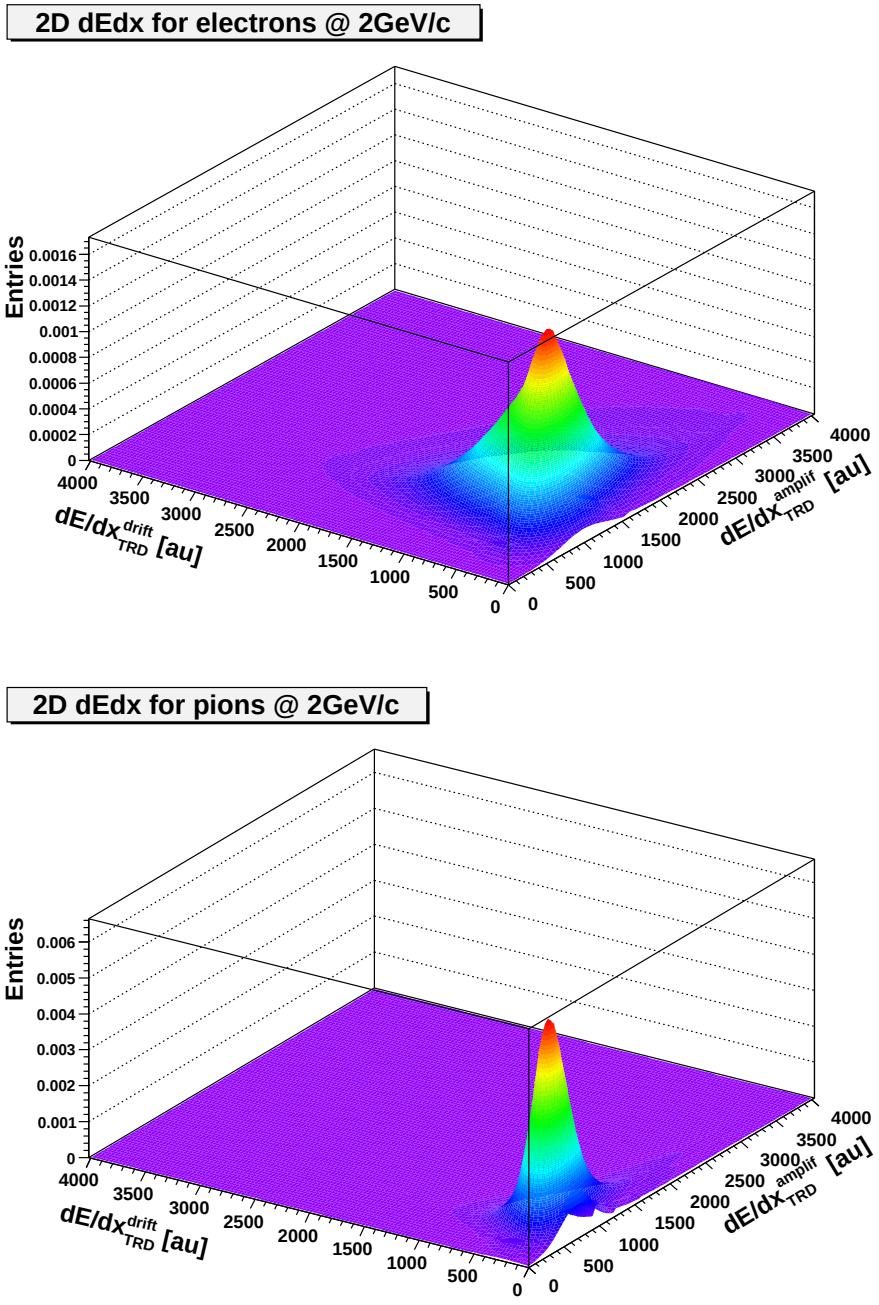

Fig. 2.13: Probability distributions for electrons and pions at a momentum of 2 GeV/c: The distributions show the likelihood value as function of charge deposit in the amplification- respectively driftregion. Both distributions have a global maximum which is for electrons at higher charge deposit values for the amplification region as well as for the drift region. Further on the width of the distribution for both charge deposit values is larger for electrons with respect to pions

3

Tools for the Analysis of simulated Proton-Proton collisions with the AliRoot framework

In order to analyse simulated and later measured data, the AliRoot framework provides a powerful package which is called the ALICE Analysis framework. The main advantages are that it allows simple data handling and it can be used for a distributed analysis.
In order to perform an analysis using the Analysis framework, an analysis task deriving from AliAnalysisTask has to be created. An analysis manager supervises the performance of the task and the data input and output. In this way it is possible to run either one single task alone or combine several tasks to an analysis train. In the analysis train it is also possible to link input and output from different tasks. Four virtual functions have to be implemented for each task: ConnectInputData, CreateOutputObject, Exec and Terminate. The first two functions are dealing with the data input and output. In the third function, the analysis code is placed. For the finalization of a task, the function Terminate has to be used. The reason for this concept is that the analysis tasks should be ready to run as distributed analysis on PROOF [1] clusters or on the ALICE GRID. In this case the data connection and the data processing has do be done on each worker node, so the first three functions have to be called on each worker. The analysis of the processed data has to be done afterwards on the master node. For the evaluation of reconstructed events a Chain of ESD-

[1] Parallel ROOt Facility: A cluster software for distributed analysis based on root. The software is designed to process root trees. Output objects are created on each worker. They have to be merged in the end.

trees[2] has to be created. The distribution of ESD events to the task is done via an Event Handler. Also for Monte-Carlo studies there is an event handler providing the Monte- Carlo event connected with the ESD Event. The analysis manager provides an interface to the event handler for the steering macro and for the analysis task. Output objects can be stored in a container structure like a TList or a TObjArray and send to the consumer via one output channel or they can be treated individually and send via output channels for each object by itself. In the second attempt however, an output container has to be created for each object, which affects the clarity of the output. This alternative should only be taken if the output of one task should serve as input for different tasks and the inputs of the following tasks differ. In case the code has to be performed on PROOF clusters, a Merge function which merges the results coming from each worker has to be implemented for each output object. For many root classes like histogram classes which are mainly used as output the Merge functions are already implemented. After merging the output, final tasks can be performed on the master inside the function Terminate. Also a special function SlaveTerminate can be implemented. This function is called on each worker. It is of interest i.e. if files are temporarily stored on the local disks of the worker and finally have to be copied to the master node.
For studies on the PROOF cluster or on the GRID, it is proposed to pack the users code into a package which is called par-file. Such a par-file contains source- and header-files for the created user-code, a makefile, a shell script which steers the creation on the library and a setup script which loads the library into the root environment. Par-archives are loaded to every worker node, so the source code is compiled on every worker. Using par-files analysis-code can be managed for three computer platforms: local machines, PROOF-

[2] ESD = Event summary data: In order to reduce the data size, for each event a summary for physics tasks is created. Further information which is needed to calibrate the detector is stored in a calibration object inside the so called ESDfriend. The access to the ESDfriend happens via the ESD object

clusters and the GRID. Especially when an analysis job contains more than one source file, par-archives become necessary.
The analysis framework is also well suited for calibration tasks, i.e. the tracking efficiency calculation is performed using the analysis framework. For the TRD a package containing tasks for efficiency studies is implemented as described in the previous chapter, and can be extended with several other tasks for calibration and PID studies. This attempt is inspired by the calibration tasks implemented for the TPC.
The AliRoot distribution provides a further framework which is handling the efficiency correction for physical observables like the transverse momentum p_T or the rapidity y. It is called the correction framework. The correction framework is based on filling containers for each physical variable for Monte-Carlo Particles and for reconstructed tracks after the applied cuts. The containers which are created in the steering macro are provided to the analysis task by the CFmanager. The correction framework also provides objects storing cuts for single tracks, pairs, PID and other topics. These cuts can be defined in the steering macro. In this case, the selection of the tracks fulfilling the criteria is done by the CFmanager. After filling the containers during the analysis, the efficiencies can be calculated by building the ratio of the two steps. In case of more than one variable, it is also possible to create an efficiency map.
V0s, kinks and cascades are reconstructed during tracking and stored in the ESD-tree. For V0 reconstruction there are two methods performed. The On-the-Fly method, which is performed during TPC tracking and the offline method performed on all tracks after tracking. The offline V0 finder regards all combinations of pairs of ESD tracks as long as they have different charge signs as V0 candidates and applies cuts on the χ^2, the Distance-to-Closest-Approach and the distance to vertex. In the On-the-Fly V0 finder, an assumption is made whether tracks are primary tracks or not. Only non-primary tracks are used for further V0 reconstruction, where also cuts on the quanti-

ties mentioned for the Offline V0 finder are applied. For all the V0s stored inside the ESD tree, the assumption for the prior particle to be a K_s^0 is done by default. However the selection of the particle has to be done during the analysis using PID information for the decay products. For the PID appropriate cuts have to be set. Further cuts have to be applied on other quantities, for example the invariant mass of the system, the track status, the Distance-to-Closest-Approach or the χ^2.

It is also possible to reconstruct particles afterwards during the analysis. This can be done using Kalman-filter approach. A special class AliKFParticle inside the AliRoot distribution provides the necessary functionality for this. The reconstruction of particles during the analysis is important especially for short living particles like hadrons containing heavy flavour like B-, D-mesons or quarkonia. It is also necessary for the reconstruction of particles decaying in more than two daughter particles or for particles decaying in two neutral particles which decay further. An example for this is the decay

$$\pi^0 \rightarrow \gamma\gamma$$

where γs are identified by γ-conversion inside ITS, TPC or TRD.

4

Measurement of p_T-spectra in pp-collisions with the ALICE Central Barrel Detectors

p_T-Spectra measured in pp-collisions are of special interest as reference distributions for the investigation of heavy ion collisions. In order to calculate the Nuclear Modification Factor (eq. 1.8) for one particle species in lead-lead collisions, the p_T-spectra for a particle species measured in proton-proton collisions serves as a normalisation together with the number of collisions in heavy-ion collisions. According to this p_T-spectra in pp-collisions have to be measured. For the studies shown below a Monte-Carlo production which was performed at GSI was used. In this production proton- proton collisions at a Centre of Mass Energy of 10 TeV were simulated using PYTHIA version 6.214 as event generator. The Centre of Mass Energy used in the simulation corresponds to the Centre of Mass Energy for the first physics runs at LHC. The production was done with the AliRoot versions 4.13. In total $3.4 \cdot 10^6$ events were analysed. The analysis was done using the ALICE Analysis Framework described above.

4.1 p_t-spectra for charged particles produced in pp-collisions at a Centre of Mass-Energy of 10 TeV

For the investigation of the p_T-spectra of the charged particles, cuts on the PID probability were made to a probability above 75% for all particle type in order to avoid contamination due to misidentification. The PID-Signal was taken as Bayesian probability of the PID signals of the central barrel detectors.

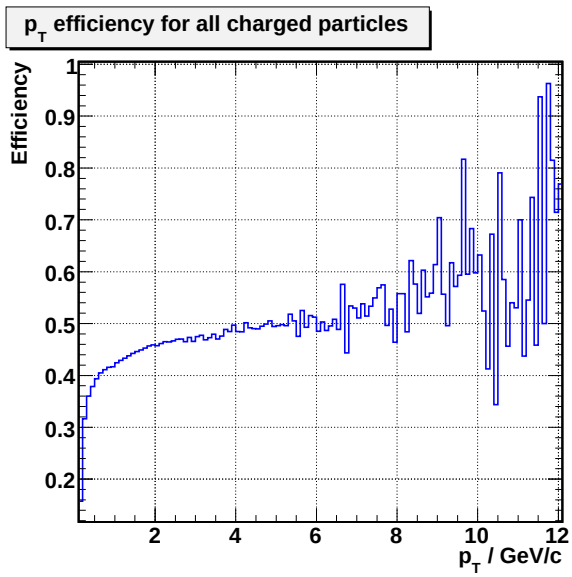

Fig. 4.1: Efficiency map for all charged particles with respect to the transverse momentum: One can see an increase of the efficiency with increasing momentum. The noisy structure above 10 GeV/c is due to the low yields of tracks in this p_T- region.

In order to profit from the electron-hadron separation capabilities of the TRD, first the PID Signal in the TRD was checked. If the PID-probability given by TRD is highest for electrons, and if the PID-probability is above 75%, then the particle is assumed to be an electron. A further cut is applied to the number of clusters inside ITS: It is expected that a track has six ITS clusters in order to be accepted. p_t-Spectra of reconstructed tracks are then compared to p_T-spectra of Monte-Carlo tracks. A requirement for Monte-Carlo tracks to be accepted was that they leave at least track references inside the TPC. The PID information for Monte-Carlo tracks is taken using the PDG code of the in the Monte-Carlo particle.

The sample is divided into two parts with similar numbers of events. The first sample was used to calculate the efficiency for the identification of a particle species using the cuts discussed above as function of the transverse momentum. The efficiency map is used afterwards to correct the p_T-spectra created using the second sample. After the correction for inefficiency, the recon-

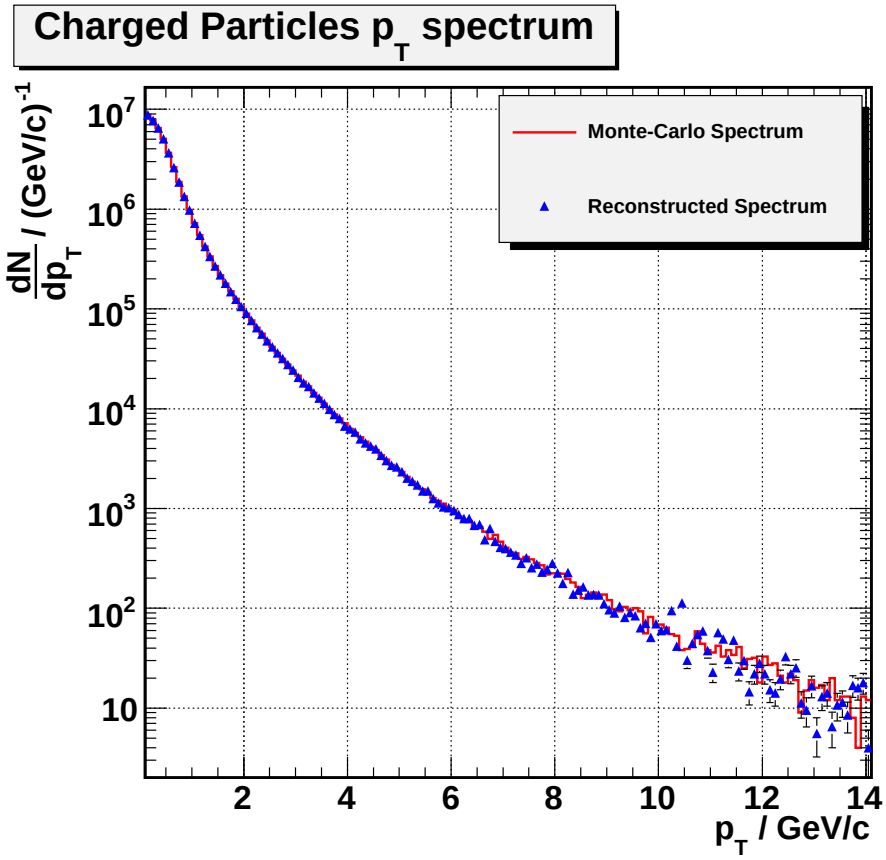

Fig. 4.2: p_t-spectrum of all charged particles passing the central barrel. The spectrum is corrected for inefficiency using the efficiency map shown in Fig. 4.1.

structed p_T-spectra can be compared to the p_T-spectra created from Monte-Carlo tracks.

Fig. 4.1 shows the efficiency as function of the transverse momentum for all charged particles with respect to the transverse momentum. One can see an increase of the efficiency with increasing transverse momentum. Above 10 GeV/c the low statistics for high-p_T tracks affects also the efficiency. One can see this from the noisy structure at higher p_t- values. The corrected p_T-spectrum for all charged particles is shown in Fig. 4.2. One can see that the reconstructed spectrum reproduces the spectrum using the Monte-Carlo data very well in the p_T-range up to 14 GeV/c.

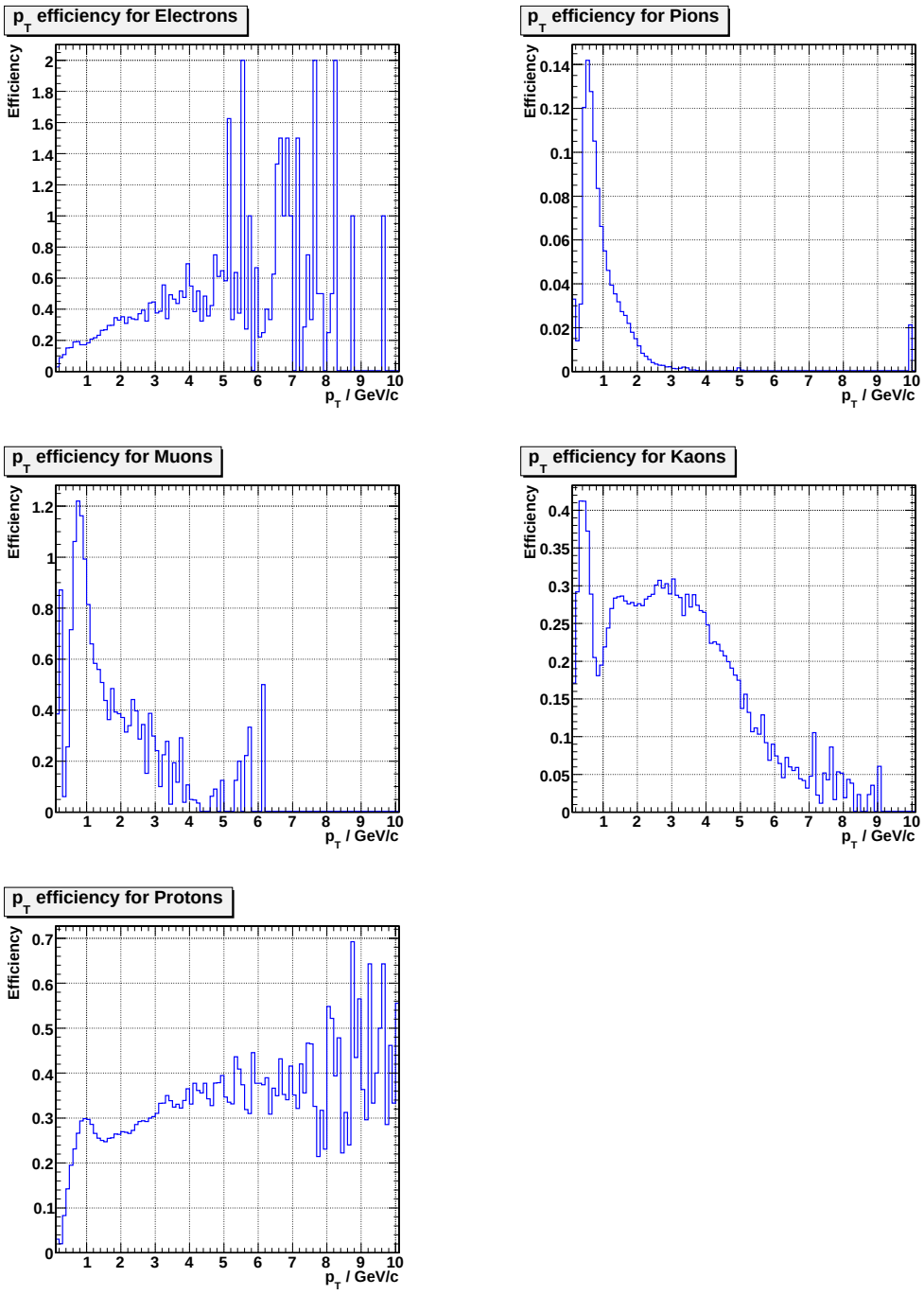

Fig. 4.3: Efficiency maps for the particle species electron, pion (upper row), muon, kaon (middle row) and proton: One can see that the efficiency for electrons increases with increasing p_T. The decrease of the efficiency for pions and muons is due to smaller PID probabilities at higher momenta. Kaons profit from the TOF PID, which leads to a second maximum in the efficiency at around 3 GeV/c.

The efficiency as function of the transverse momentum is shown in Fig. 4.3 for the different charged particle species. From the efficiency plots one can see an increase of the efficiency for electrons and protons towards higher transverse momenta, while for pions, muons and kaons the efficiency decreases towards higher momenta. The identification of pions and muons is based on the energy loss inside the TPC. Since the particles have similar mass, the distinction of pions and muons becomes more difficult with increasing momentum, which leads to similar PID probabilities for muons and pions. According to the cuts applied on the PID, the yields of identified pions and muons decrease with higher momentum. This explains the decrease of the efficiency for pions and muons. For kaons one can see beside the maximum at 0.5 GeV/c a local maximum of the efficiency at a transverse momentum of 3 GeV/c. The first peak is due to the kaon identification using TPC PID at lower momenta, the second maximum reflects the p_T-region where the kaon identification using TOF PID information is best. So in the p_T-region above 2 GeV/c the main contribution to the kaon identification comes from TOF PID. Protons also profit from the particle identification inside TOF. Here one can see an increase of the efficiency with increasing p_T. At 10 GeV/c one can determine an efficiency of 0.5. Also for electrons an increase of the efficiency can be seen. Here in the region above 2 GeV/c, the identification of electrons profit from the TRD PID.

Fig. 4.4 shows the p_T-spectra for the particle types pion, electron, muon, kaon and proton after the correction for inefficiency. In each picture the reconstructed spectrum is compared to the Monte Carlo spectrum. One can see that the Monte-Carlo spectra can be reproduced well with the efficiency-corrected reconstructed data up to a transverse momentum of 6 GeV/c. For the species electrons, kaons and protons, the reconstructed p_T-spectrum and the p_T-spectrum from Monte-Carlo tracks agree well also up to higher transverse momenta (8 GeV/c in case of electrons and kaons and 14 GeV/c in case of protons).

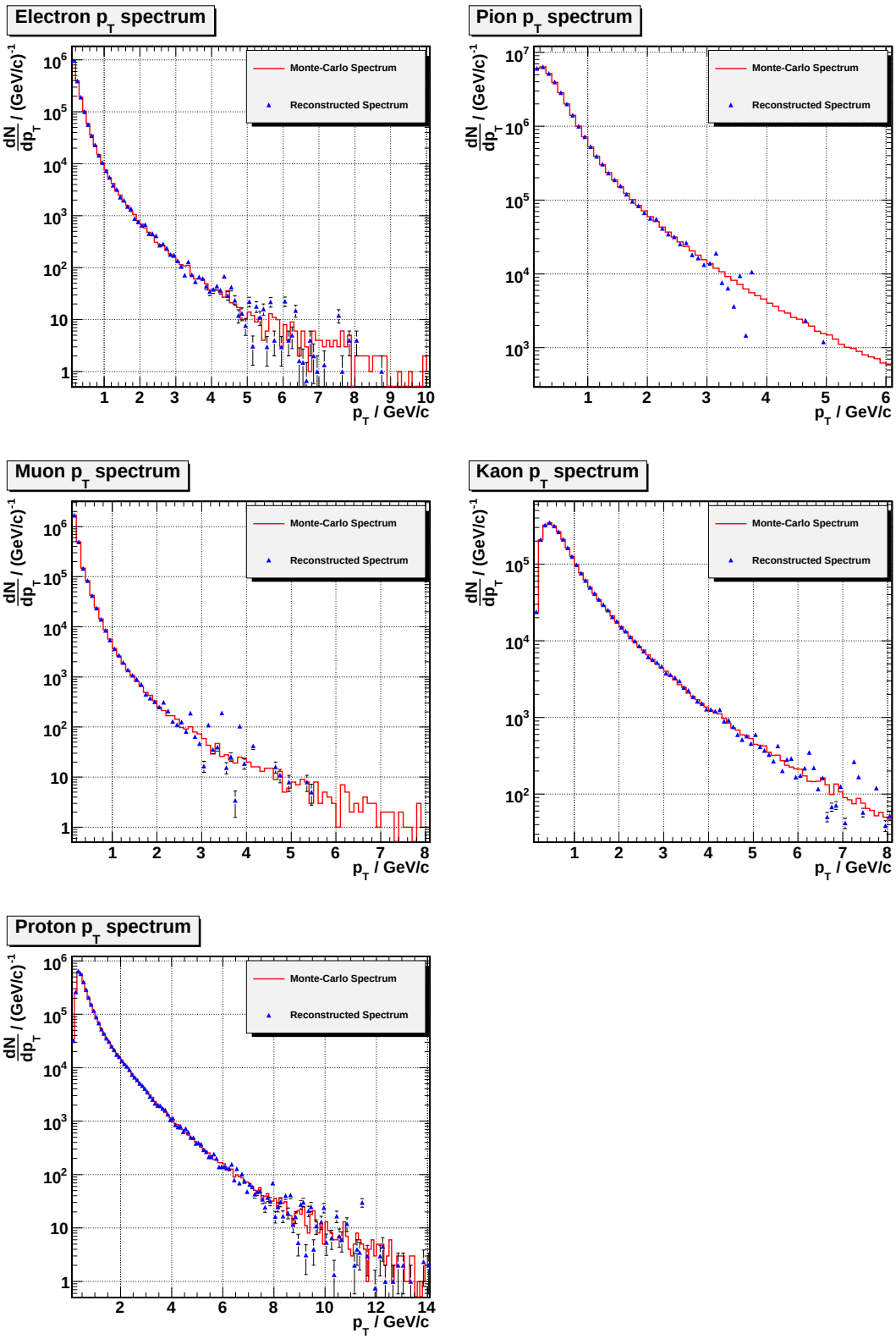

Fig. 4.4: p_T-spectra for the particle species pion, electron, muon, kaon and proton. Shown are the p_T-spectra derived from Monte-Carlo tracks and the p_T-spectra from measured tracks for each species. The reconstructed spectra are corrected for inefficiency. One can see that in the p_T-region up to 6 GeV/c the reconstructed spectra reproduce the Monte-Carlo spectra very well.

An interesting point is that in contrast to the spectra for electron, muons and pion, which have their maximum below a transverse momentum of 100 MeV/c, the kaon p_T-distribution has a peak at around 300 MeV/c. Also for protons a peak at around 300 MeV/c can be seen. Since the particle p_T-spectra can be described with a Maxwell-Boltzmann distribution, the peak can be explained with a higher energy which kaons and protons are transporting with respect to the lighter particle species. Since electrons, muons and pion are the product of decays, they carry only a fraction of transverse momentum, which also explains their maximum at very low p_T.

4.2 p_t-spectra of K_s^0 and Λ produced in pp-collisions at a Centre of Mass Energy of 10 TeV

K_s^0 can be identified by their decay into two pions

$$K_s^0 \rightarrow \pi^+\pi^- \tag{4.1}$$

with a branching ratio of 69%[11]. Λ can be reconstructed according their decay into a pion and a proton

$$\Lambda \rightarrow \pi^- p$$

with a branching ratio of 63.9%. The particles were reconstructed using the On-the-Fly V0 finder. As PID signal the combined PID of all detectors was used. Cuts on the PID probability were set to 75%.

Fig. 4.5 shows the invariant mass spectra for $\pi\pi$. One can see a sharp peak at $0.49 GeV/c^2$. This peak can be identified with the particle K_s^0. Mass and width are derived from a gaussian fit to $m_{K^0} = 499.6 MeV/c^2$ and $\Gamma_{K^0} = 3.5 MeV/c^2$. Fig. 4.6 show the invariant mass spectrum for πp in a region between 1.0 and $1.2 GeV/c^2$. Here one can see a clear peak at an invariant mass of $1.116 GeV/c^2$, which can be identified with the particle Λ. Mass an width can be derived from a Lorentz fit to $m_\Lambda = 1.1161 GeV/c^2$ respectively $\Gamma_\Lambda = 1.519 MeV/c^2$.

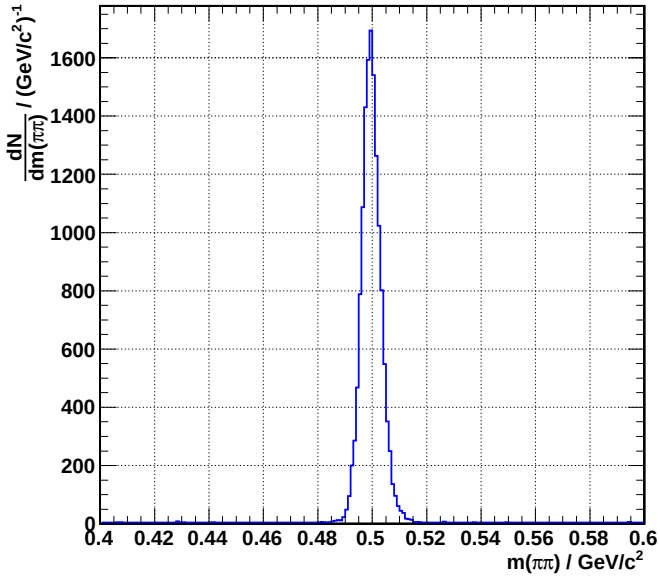

Fig. 4.5: Invariant mass spectrum for $\pi\pi$ in the region between 0.4 and $0.6 GeV/c^2$. One can see a sharp peak at an invariant mass of $0.49 GeV/c^2$. This peak can be identified with the particle K_s^0.

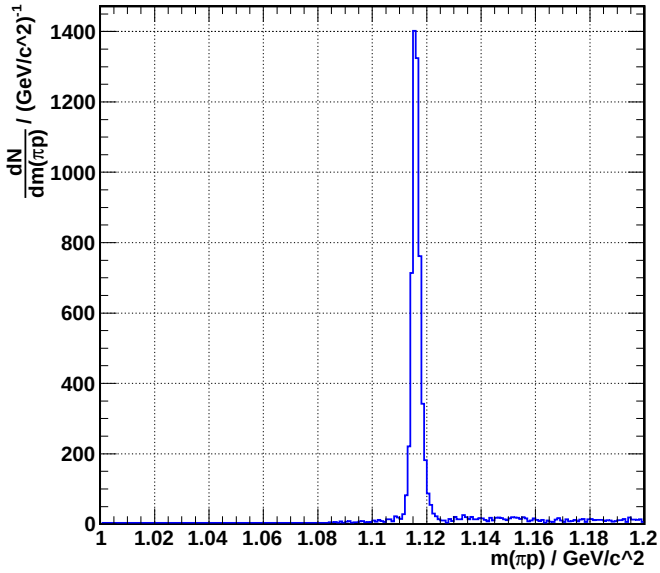

Fig. 4.6: Invariant mass spectrum for the channel πp in the region between $1.0 GeV/c^2$ and $1.2 GeV/c^2$: One can see a sharp peak at an invariant mass of $1.1 GeV/c^2$. This peak can be identified with the particle Λ.

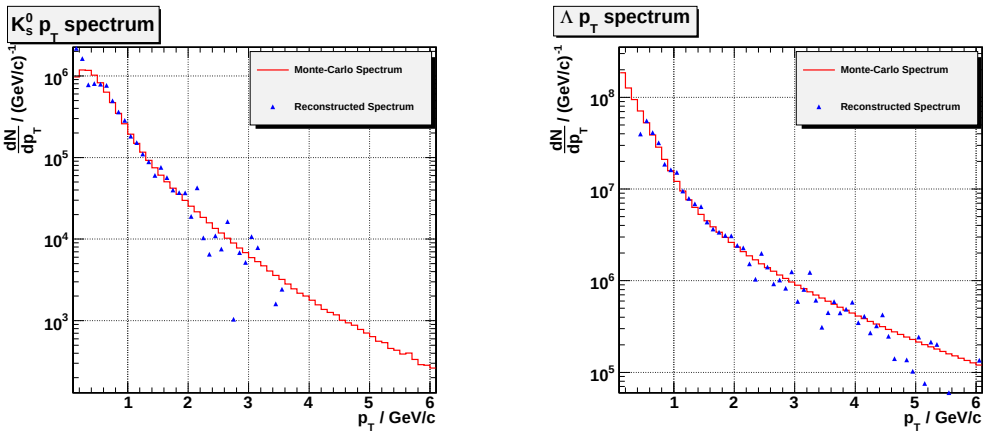

Fig. 4.7: p_T-spectrum for K_s^0(left) and Λ: Shown are the reconstructed spectra (blue) and the spectra derived from Monte-Carlo tracks (red). The reconstructed spectra are corrected for inefficiency. One can see that the reconstructed spectra reproduces the spectra created using Monte-Carlo tracks well up to a transverse momentum of 3 GeV/c for K_s^0 respectively 6 GeV/c for Λ

Fig. 4.7 shows the p_T-spectra for K_s^0 and Λ. Here the reconstructed spectra after correction for inefficiency and the spectra derived from Monte-Carlo tracks are presented. The efficiency plots are shown in the appendix (Fig. B.1). There one can see that the efficiency stays below 1% for K_s^0 and Λ in the p_T-region which was investigated. Influences on the efficiency are coming from the cuts on the PID probability and from cuts inside the V0 finder. The reconstructed p_T-spectra for K_s^0 and Λ after efficiency correction reproduce the spectra derived from Monte-Carlo tracks very well up to a transverse momentum of 3 GeV/c in case of K_s^0 and up to 6 GeV/c in case of Λ. In order to increase the efficiency, one can lower the cuts on the PID probability and accept misidentification. A further possibility is to reconstruct the V0s again out of all tracks which are identified as pions using the AliKFParticle class. Here cuts have to be applied on the Distance-to-Closest-Approach and on the distance of the decay vertex to the primary vertex in order to reduce the background.

5

Summary and Outlook

Between October 2007 and January 2008 the TRD tracking code was completely restructured and tested using data from the November 2007 testbeam. In the time between January 2008 and July 2008 also the quality of the TRD tracking was checked. The focus is on the efficiency and on the position resolution in Monte-Carlo studies. It has been shown that the efficiency of TRD stand alone tracking and combined TRD stand alone and barrel tracking is above 90% with respect to all the findable tracks. For the position error it has been shown that the distance between Monte-Carlo track and reconstructed track increases with the track angles ϕ and θ and has minimal values in the order of $150\mu m$ in y-direction respectively 3mm in z-direction. Concerning the cluster residuals with respect to tracks which were measured using cosmic events, one can see a saturation at $750\mu m$ in y- direction. Further effort is needed to achieve a value of about $400\mu m$ reached with prototypes [4].
The reconstructed p_t-spectra for all charged particles after the correction for inefficiency reproduce the p_T-spectrum derived from the Monte-Carlo tracks very well up to a transverse momentum of 14 GeV/c. Here the efficiency increases with increasing momentum and reaches a value of 0.6 at 10 GeV/c. For the species electron, pion, proton, muon and kaon the p_T- spectrum derived form Monte-Carlo tracks can be reproduced by the reconstructed p_T-spectrum after efficiency-correction up to a transverse momentum of 6 GeV/c. The efficiency decreases for muons and pions and increases for protons and

electrons. The effect could be explained with difficulties in the separation of muons and pions for high momenta using the TPC, while the electron respectively proton PID-signal could be improved using the detectors TOF for protons and TRD for electrons. The local maximum of the efficiency for the kaons at 3 GeV/c can also be explained by an improvement in the PID signal due to the TOF-PID in this p_T-region. In the higher p_T-region a larger statistics is needed in order to draw conclusions on the efficiency and the shape of the p_T-spectra. Concerning uncharged hadrons it has been shown that K_s^0 and Λ can be reconstructed in ALICE using the On-The-Fly V0 finder. Here the reconstructed p_T-spectra reproduce the p_T-spectra from Monte-Carlo tracks up to a transverse momentum of 3 GeV/c for K_s^0 respectively 6 GeV/c for Λ. In both cases however the efficiency is rather low.

For the cosmic run in August 2008 and the first beam-gas collisions, the main tasks are to optimize the TRD reconstruction parameters and to verify the TRD position resolution and the cluster residuals. This parameter set will be employed in the reconstruction of the data of the first physics runs. Also the measured position resolution is of high importance for the first physics runs.

Appendix

A

Fundamentals of heavy ion collisions

In order to characterize the dynamics of relativistic particles in heavy ion experiments, new quantities are introduced. A very usefull quantity is the rapidity. The rapidity is defined in the following way[19]:

$$y = \frac{1}{2} \ln \left(\frac{p_0 + p_z}{p_0 - p_z} \right) \tag{A.1}$$

Here p_0 is the energy of a particle and p_z is the z-component of the momentum of the particle. A good choice for the z-direction is the beam direction. With the help of the rapiditiy we can express the energy respectively z-component of the momentum of a particle:

$$p_0 = m_T \cosh y \tag{A.2}$$

$$p_z = m_T \sinh y \tag{A.3}$$

where m_T is defined as the transverse mass of the particle $m_T^2 = m_0^2 + p_T^2$. However, in some experiments, it is not possible to measure both quantities energy and momentum in beam direction for a particle, but only the angle relative to the beam axis. Therefore a new quantity which is called pseudorapidity is introduced. The pseudorapidity is defined in the following way:

$$\eta = -\ln \left[\tan \left(\frac{\theta}{2} \right) \right] \tag{A.4}$$

whith the angle θ of the particle track with respect to the beamline. With the help of the momenta, the pseudorapidity can also be expressed in the following way:

$$\eta = \frac{1}{2} \ln \left(\frac{|p| + p_z}{|p| - p_z} \right) \tag{A.5}$$

As can be seen from the comparison of eq. A.1 and eq. A.5, the pseudorapidity approximates the rapidity for large momenta $\underline{\mathrm{p}} \approx p_0$. Now it is also possible to express the absolute value of the momentum and the z-component with the help of the pseudorapidity:

$$|p| = p_t \cosh \eta \tag{A.6}$$

$$p_z = p_t \sinh \eta \tag{A.7}$$

with the transverse momentum $p_T = \sqrt{p^2 - p_z^2}$, which is the absolute momentum orthogonal to the z-direction.

B

Efficiency Maps for K_s^0 and Λ

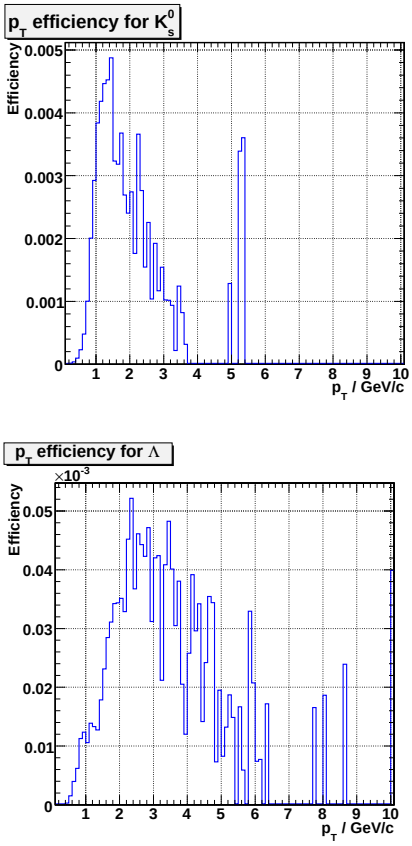

Fig. B.1: Efficiency for the reconstrucion of K_s^0 and Λ as function of the transverse momentum: One can see that the efficiency reaches its maximum for K_s^0 and Λ at approximately 2GeV/c. In both cases the efficiency stays below 1% for the complete p_T-range which was investigated.

References

[1] ALICE Collaboration. The ALICE Offline Bible. http://aliceinfo.cern.ch/export/download/OfflineDownload/OfflineBible.pdf.

[2] ALICE Collaboration. ALICE: Physics Performance Report, Volume I. *Journal of Physics G Nuclear Physics*, 30:1517–1763, November 2004.

[3] ALICE Collaboration. ALICE: Physics Performance Report, Volume II. *Journal of Physics G Nuclear Physics*, 32:1295–2040, September 2006.

[4] R. Bailhache and C. Lippmann. New test beam results with prototypes of the ALICE TRD. *Nuclear Instruments and Methods in Physics Research A*, 563:310–313, July 2006.

[5] S. A. Bass, M. Gyulassy, H. Stöcker, and W. Greiner. TOPICAL REVIEW: Signatures of quark-gluon plasma formation in high energy heavy-ion collisions: a critical review. *Journal of Physics G Nuclear Physics*, 25:1–57, March 1999.

[6] S. Bethke. α_s 2002. *Nuclear Physics B Proceedings Supplements*, 121:74–81, June 2003.

[7] J.-P. Blaizot. Theory of the Quark-Gluon Plasma. In W. Plessas and L. Mathelitsch, editors, *Lectures on Quark Matter*, volume 583 of *Lecture Notes in Physics, Berlin Springer Verlag*, pages 117–161, 2002.

[8] P. Braun-Munzinger. Quarkonium production in ultra-relativistic nuclear collisions: suppression versus enhancement. *Journal of Physics G Nuclear Physics*, 34:471–477, August 2007.

[9] L. V. Bravina, K. Tywoniuk, E. E. Zabrodin, G. Burau, J. Bleibel, C. Fuchs, and A. Faessler. Elliptic flow at RHIC: Where and when was it formed? [rapid communication]. *Physics Letters B*, 631:109–117, December 2005.

[10] A. Chodos, R. L. Jaffe, K. Johnson, and C. B. Thorn. Baryon structure in the bag theory. *Phys. Rev. D*, 10(8):2599–2604, Oct 1974.

[11] W.-M. Yao et al. (Particle Data Group). Particle physics booklet. *Journal of Physics G: Nuclear and Particle Physics*, 35(1), 2006.

[12] M. Fasel. Stand alone tracking in the ALICE Transition Radiation Detector, 2008. Project Proposal.

[13] Jiayun Chen (for the STAR Collaboration). Directed flow of identified particles from au+au collisions at rhic. *Journal of Physics G: Nuclear and Particle Physics*, 35(4):044072 (6pp), 2008.

[14] J. W. Harris and B. Müller. The Search for the Quark-Gluon Plasma. *Annual Review of Nuclear and Particle Science*, 46:71–107, 1996.

[15] Ulrich W. Heinz. Concepts of heavy-ion physics, 2004.

[16] T. Matsui and H. Satz. J/ψ suppression by quark-gluon plasma formation. *Physics Letters B*, 178:416–422, October 1986.

[17] M. J. Tannenbaum. Recent results in relativistic heavy ion collisions: from 'a new state of matter' to 'the perfect fluid'. *Reports of Progress in Physics*, 69:2005–2059, July 2006.

[18] A. Wilk. Analysis of the electron / pion separation capability with real size ALICE TRD prototypes using a neural network algorithm. *Nucl. Instrum. Meth.*, A563:314–316, 2006.

[19] Cheuk-Yin Wong. *Introduction to Heavy Ion Collisions*. World Scientific Publishing, 1994.

Acknowledgement

At the end of the Master Thesis I would like to thank Prof. Braun-Munzinger for giving me the opportunity to produce this Master Thesis in his group at Gesellschaft für Schwerionenforschung, Darmstadt. Also I would like to thank for the excellent supervision. Further on I would like to thank my tutors Dr. Anton Andronic and Dr. Alexandru Bercuci for many useful discussions during the time of this Master Thesis. Also I would like to thank the whole work group and the ALICE collaboration. A special thank goes to my room-mates Raphaelle Bailhache, Oliver Busch, Ana Marin and Woo Jin Park for the good working climate and the useful discussions. Also to be mentioned are special thanks to the Members of the work group and the ALICE TRD Collaboration. Also special thanks to Silvia Masciocchi for setting up an Analysis Train for the ALICE group at GSI. The train is a powerful tool for the analysis of large data sets.

Special thank go to the GSI for giving me the opportunity to work at CERN for a time during the Master Thesis.

Last but not least I would like to thank my parents for their support during the time of the Master Thesis and during the whole duration of my studies.

Erklärung zur Master Thesis
gemäß § 23 Abs. 7 APB

Hiermit versichere ich, die vorliegende Master Thesis ohne Hilfe Dritter nur mit den angegebenen Quellen und Hilfsmitteln angefertigt zu haben. Alle Stellen, die aus den Quellen entnommen wurden, sind als solche kenntlich gemacht worden. Diese Arbeit hat in gleicher Form noch keiner Prüfungsbehörde vorgelegen.

Darmstadt, den _____

_____

Unterschrift